Accepted Manuscript

Multiscale formulation for material failure accounting for cohesive cracks at the macro and micro scales

S. Toro, P.J. Sánchez, P.J. Blanco, E.A. de Souza Neto, A.E. Huespe, R.A. Feijóo

PII: S0749-6419(15)00119-9

DOI: 10.1016/j.ijplas.2015.07.001

Reference: INTPLA 1940

To appear in: *International Journal of Plasticity*

Received Date: 17 April 2015

Revised Date: 19 June 2015

Accepted Date: 3 July 2015

Please cite this article as: Toro, S., Sánchez, P.J., Blanco, P.J., de Souza Neto, E.A., Huespe, A.E., Feijóo, R.A., Multiscale formulation for material failure accounting for cohesive cracks at the macro and micro scales, *International Journal of Plasticity* (2015), doi: 10.1016/j.ijplas.2015.07.001.

Multiscale formulation for material failure accounting for cohesive cracks at the macro and micro scales

S. Toro[‡♯], P.J. Sánchez[‡♯], P.J. Blanco[§♭], E.A. de Souza Neto[♮]
A.E. Huespe[‡], R.A. Feijóo[§♭]

[‡]CIMEC-UNL-CONICET, Güemes 3450, CP 3000 Santa Fe, Argentina
[♯]GIMNI-UTN-FRSF, Lavaise 610, CP 3000 Santa Fe, Argentina
[§]LNCC/MCTI, Av. Getúlio Vargas 333, Petrópolis, RJ, CEP: 25651-075, Brasil
[♭]INCT-MACC, Instituto Nacional de Ciência e Tecnologia
em Medicina Assistida por Computação Científica, Brasil
[♮]Zienkiewicz Centre for Computational Engineering
Swansea University, Singleton Park, Swansea SA2 8PP, UK

Keywords: semi-concurrent multiscale model, material failure, crack path tortuosity, homogenization of traction-separation law, heterogeneous materials.

Abstract

This contribution presents a two-scale formulation devised to simulate failure in materials with heterogeneous micro-structure. The mechanical model accounts for the nucleation of cohesive cracks in the micro-scale domain. The evolution and propagation of cohesive micro-cracks can induce material instability at the macro-scale level. Then, a cohesive crack is nucleated in the macro-scale model which considers, in a homogenized sense, the constitutive response of the intricate failure mode taking place at the smaller length scale.

The two-scale semi-concurrent model is based on the concept of *Representative Volume Element* (RVE). It is developed following an axiomatic variational structure. Two hypotheses are introduced in order to build the foundations of the entire theory, namely: (i) a mechanism for transferring kinematical information from macro-to-micro scale along with the concept of "*Kinematical Admissibility*", and (ii) a *Multiscale Variational Principle* of internal virtual power equivalence between the involved scales of analysis. The homogenization formulae for the generalized stresses, as well as the equilibrium equations at the micro-scale, are consequences of the variational statement of the problem.

The present multiscale technique is a generalization of a previous model proposed by the authors [1, 2] and could be viewed as an application of a recent contribution [3]. The main novelty in this article lies on the fact that failure modes in the micro-structure involve a set of multiple *cohesive cracks*, connected or disconnected, with arbitrary orientation, conforming a complex tortuous failure path. Following the present multiscale modeling approach, the tortuosity effect is introduced as a kinematical concept and has a direct consequence in the homogenized mechanical response.

Numerical examples are presented showing the potentialities of the model to simulate complex and realistic fracture problems in heterogeneous materials. In order to validate the multiscale technique in a rigorous manner, comparisons with the so-called DNS (Direct Numerical Solution) approach are also presented.

community. Current methodologies could be grouped in two families:

(i) The *cohesive surface approach to fracture*, where the fracture process zone (FPZ) is condensed into a cohesive interface with displacement jumps across it. A "discrete-type" constitutive law is prescribed to characterize the evolution of the *cohesive traction* with respect to the *displacement jump* on the crack faces, see [4, 5] and the references cited therein.

(ii) The *continuum approach to fracture*, where regularized "continuum-type" *stress-strain* theories are used to characterize the response of the solid including the FPZ, which is idealized as narrow bands with intense strain-localization and material softening [6–8].

Some attempts to link both methodologies have been proposed in the literature, see for example [9–12].

These two families of models can be grouped into a more comprehensive category, named the *phenomenological approach to failure mechanics*. In this context, the "discrete" as well as the "continuum-type" constitutive relations consider one single length scale of analysis (mono-scale analysis). Thus, degradation micro-mechanical effects can only be regarded partially, either by introducing internal variables (see [13] and references cited therein) or additional kinematical descriptors [14, 15]. In spite of its computational appeal, this class of methodologies has serious limitations. For arbitrary loading histories, it is not a trivial task to determine the format or structure of macroscopic laws with the ability to capture complex failure phenomena taking place at smaller length scales. Major challenges in the development of phenomenological models for material failure are: (i) the characterization of material parameters and internal variable evolution laws, via well-defined experimental tests, and (ii) the rigorous formulation of the mechanical model, within a thermodynamically consistent framework.

With the aim of circumventing the drawbacks of phenomenological approaches to material modeling in general, and fracture mechanics modeling in particular, an alternative paradigm can be employed: the so-called *multiscale approach* [16, 17]. This paradigm incorporates the heterogeneous micro-structure in the formulation of the macroscopic constitutive model through the *homogenization* concept. The idea is intuitive and comes from the early days of material modeling science [18–23]. The crucial assumption is to remove the constitutive definition at the macroscopic level and defining it at a smaller length scale, where the behavior of each of the material micro-constituents and their interactions are characterized. Then, by using averaging techniques, an overall constitutive response is transferred to the larger scale. Following this concept, effective material behaviors can be retrieved from the intricate interactions between geometry and constitutive behavior of all micro-structural components occurring at the smaller scale.

Among the many different multiscale strategies available at present (see for example [19, 22, 24–29]), two-scale semi-concurrent models based on the concept of Representative Volume Element (RVE) have reached an acceptable degree of generality [30–38]. Such models link the macro-scale with a smaller length scale, the micro-scale, where heterogeneities and their corresponding interaction laws are identifiable. The present contribution follows this particular class of multiscale (two-scale, RVE-based) formulation.

Material failure is a phenomenon strongly dependent on the underlying material heterogeneity, since the evolution of degradation mechanisms is influenced by micro-structural details, as for example the presence of voids, inclusions, fibers, interfaces between aggregates, etc. Thus, the RVE-based multiscale paradigm adapts very well to this kind of problem [39, 40]. However, material failure phenomenology introduces serious theoretical issues in the development of RVE-based techniques, demanding a careful study. In fact, material degradation observed at macro-scale is a consequence of strain localization processes along with loading/unloading mechanisms taking place at different regions of the micro-scale. Classical multi-scale procedures, such as those cited in the previous paragraph, postulate uniform distribution of macro-scale strains into the micro-scale domain as well as standard homogenization rules for stresses, i.e. volumetric average extended over the entire RVE. However, during the failure regime, these asumptions have a very debatable physical meaning. New definitions and novel homogenization techniques need to be introduced when strain localization phenomena are present.

One additional key issue that must be clarified is the lack of *objectivity* of the homogenized response, with respect to the RVE-size, when classical homogenization procedures are employed [1, 41, 42]. This is due to the well-known size-effect phenomenon, inherent to structural failure mechanics [43]. Some recent contributions have addressed this important theoretical limitation of the classical multiscale models, invoking unconventional homogenization rules, see for example [1, 3, 42, 44–47].

Due to all difficulties exposed above, the use of RVE-based techniques to simulate material failure is relatively new [47–53].

accounting for the nucleation and propagation of cohesive cracks at the micro-scale which may induce crack nucleation and propagation at the macro-scale level, from an initially continuum (unfractured) medium. Following conventional RVE-based approaches, the constitutive modelling at the macro-scale is not characterized through explicit functions. Instead, they are determined as a result of a well-defined homogenization procedures gathering information from the smaller length scale. These homogenization procedures, or scale-transition equations, evaluate the macro-scale stress and traction by means of stresses and tractions observed at the micro-scale. Then, the methodology only requires the explicit definitions of specific (phenomenological) constitutive relations for every component identified at the micro-scale.

The discussion focuses around the theoretical foundations of the multiscale methodology, and scale-transition equations, emphasizing the mechanism for transferring kinematical information between the macro and micro-scales when material failure is involved. Kinematics is the cornerstone of the present approach. The minimum number of hypotheses, needed to develop the entire multiscale theory, are stated and justified. In this sense, two postulates define the multiscale formulation:

- (H1) The definition of the kinematics at the macro and micro-scales, along with the so-called *Kinematical Admissibility* requirement [3] that both kinematics have to meet.

- (H2) A Principle of Multiscale Virtual Power [3]. It is an adapted (variational) version of the Hill-Mandel principle of macro-homogeneity [21, 54], which includes the internal virtual power contribution from cohesive cracks at both scales[1].

Then, by enforcing the variational statement given by hypothesis (H2), the following consequences arise naturally:

- (C1) The stress homogenization formula, for macro-scale points in the bulk (unfractured) material.

- (C2) The cohesive traction homogenization formula, for points on the macro-scale crack interface.

- (C3) The equilibrium problem at the micro-scale for both macro-mechanical regimes: fractured and unfractured.

This work generalizes the *Failure-Oriented Multiscale Formulation* (FOMF) proposed by the authors in [1, 2, 55]. The FOMF was originally developed to obtain macro-scale cohesive constitutive laws from microstructures with straight *strain-localization softening-bands of finite thickness*, regularized through the smeared crack approach. Novel ideas of the present contribution are:

- The FOMF is extended to the analysis of materials in which micro-scale failure mechanisms are modeled by the nucleation and propagation of *"cohesive micro-cracks"*[2]. Since the kinematics at the micro-scale differs from that reported in [1, 2, 55], the specific assumptions adopted in H1 and H2 must be consistently reformulated. The issue of introducing multiple kinematical discontinuities at the micro-scale domain is analyzed in detail. We show that the present model can be regarded as the limit case of strain-localization bands at the RVE when the thickness of the strain-localization sub-domains approaches to zero. Another important point is that cohesive constitutive laws characterized at the RVE level could be viewed as the effective response of a FPZ existing in a yet smaller length scale. In this way, the present model can be considered as an intermediate step towards a multiscale approach with more than two scales of analysis to material failure.

- The second contribution aims to capture more general crack patterns and complex failure geometries at the RVE. From a physical point of view, cracks at the micro-scale can display zig-zag-like trajectories. They propagate towards weaker defects and tend to divert from rigid material inclusions. Thus, in real applications, the crack path can be tortuous. The level of tortuosity at the micro-scale has a direct impact at the macroscopic response [56]. As the crack path tortuosity increases, the effective dissipated energy tends to increase (examples are presented in Section 5). The micro-crack tortuosity is introduced in the present model during the insertion of macro-scale kinematics into the RVE-domain. Furthermore, since

[1] It is worth noting that statement H2 depends on H1, in the sense that H1 defines the kinematically admissible fields which play a role in the variational problem established through H2, see Section 3.3 for more details.

[2] Both, cohesive cracks and finite thickness softening bands could be modeled in the RVE domain. However, in this paper, we focus on modeling cohesive interfaces.

In summary, the remarkable advantage of using RVE-based multiscale model to simulate material failure is that simple interactions and failure mechanisms developed at the micro-scale level can be taken into account for capturing complex overall constitutive relations at the macro-scale during the material failure regime. These complex macro-scale models are not affordable with phenomenological mono-scale material failure models. On the other hand, a disadvantage of RVE-based multiscale model in contrast to mono-scale material models is that the computational cost is highly demanding. Then, the development of reduced order models to make the computation affordable may be compulsory [52].

The remainder of this paper is organized as follows. Section 2 describes the macro-scale governing equations for problems involving cohesive cracks. In Section 3, a variationally consistent procedure to develop the scale bridging technique, from macro-to-micro scales, is discussed in detail. Such methodology is consistent with the mechanical process of loading-unloading branches taking place at the macro-scale once a cohesive crack is nucleated. Section 3 presents the key theoretical aspects of the paper. Numerical implementation issues are briefly discussed in Section 4. The discrete model is assessed and validated through numerical simulations in Section 5. Rigorous comparisons between the proposed multiscale model and Direct Numerical Simulations (DNS) are presented. Conclusions are presented in Section 6. Two appendices are also included, which show specific details of the proposed multiscale model and some auxiliary calculations.

2 Macro-scale model

The solid at the macro-scale is idealized as a continuum with an heterogeneous micro or meso-structure, where macro-scale displacements, macro-scale strains and macro-scale stresses ($\boldsymbol{u}, \boldsymbol{\varepsilon}, \boldsymbol{\sigma}$, respectively) characterize the mechanical state of the body. A cohesive macro-crack is nucleated once a critical material state is reached. Thus, new independent variables are required to properly describe the mechanical behavior of the medium: (i) an additional kinematical descriptor, $\boldsymbol{\beta}$, accounting for the displacement jump acting across the crack faces and (ii) a cohesive traction, $\boldsymbol{T}$, the dual power-conjugate quantity to the displacement jump.

In this section, the macro-scale governing equations for the cohesive crack model are introduced, covering kinematics, equilibrium and the need for two constitutive relations (for the stresses and cohesive tractions). In particular, whenever the constitutive responses are required, a transition procedure towards a smaller length scale is proposed instead of using conventional phenomenological approaches based on macroscopic laws. The transition scale mechanism is developed in Section 3.

With this idea in mind, it is assumed that every point in the macro-scale domain is associated with a Representative Volume Element (RVE).

The RVE concept also applies for points located on a cohesive macro-crack, see Fig. 1. For these points, the problem formulation involves a constitutive link between a *surface domain* at the macro-scale (the macro-crack) and a *volume domain* at the micro-scale (the RVE). Therefore, a consistent scale transition technique dealing with such dimensional heterogeneity between scales has to be developed.

The so-called scale separation requirement is assumed, in the sense that the RVE-characteristic length, here denoted as ℓ_{RVE}, is much smaller than the characteristic length at the macro-scale ℓ ($\ell_{RVE} \ll \ell$), see Fig. 1. Moreover, the RVE-size must be large enough to ensure a statistically representative distribution of heterogeneities.

2.1 General definitions and nomenclature

Let be given a solid identified, at the macro-scale, with an open/bounded domain Ω in the Euclidean space $\mathbb{R}^{nd}$, nd is the spatial dimension of the problem. The boundary of Ω is Γ, with outward normal unit vector $\boldsymbol{\nu}$. Prescribed displacements, $\boldsymbol{u}_D$, are applied on $\Gamma_D \subset \Gamma$, whereas predefined external tractions, $\boldsymbol{t}^e$, are imposed on $\Gamma_N \subset \Gamma$ ($\Gamma_D \cup \Gamma_N = \Gamma$ and $\Gamma_D \cap \Gamma_N = \emptyset$), see Fig. 1.

Points at the macro-scale are labeled by their coordinates, denoted "$\boldsymbol{x}$". A monotonically increasing pseudo-time variable $t \in [0, \tau]$ is used to account for the evolution of the nonlinear material response, where τ represents the final stage of analysis.

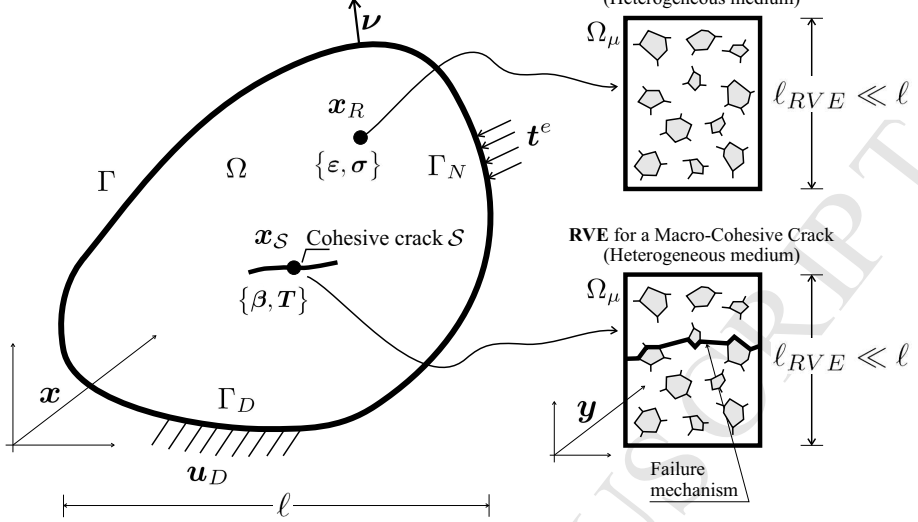

Figure 1: Transition-scale idealization for points with different mechanical conditions at the macro-scale: pre-critical (continuum) and post-critical (cracked) regime.

2.2 Kinematical description

Initially, the body is unfractured and the kinematics in Ω is continuous. However, during the loading history, a macro-scale cohesive crack, denoted $\mathcal{S}$, is nucleated at a specific time $t_N \in [0, \tau]$[3]. A point belonging to $\mathcal{S}$ is denoted $\boldsymbol{x}_{\mathcal{S}}$, whereas a point belonging to the continuous part of the solid $(\Omega \backslash \mathcal{S})$ is denoted $\boldsymbol{x}_R$, see Fig. 1. Subscript $(\cdot)_R$ means that the kinematics at $\boldsymbol{x}_R$ is "regular".

A proper criterion to determine the macro-crack nucleation time $t_N \in [0, \tau]$, at each point $\boldsymbol{x}_R$ in the macro-scale, is required. For example, as suggested in [1, 2, 55], the classical discontinuous bifurcation analysis applied to the homogenized localization tensor, denoted by $\boldsymbol{Q}$, can be used. The second orden tensor $\boldsymbol{Q}$ is defined as:

$$\boldsymbol{Q} = \left[\boldsymbol{C}(\boldsymbol{\varepsilon}(t))\, \boldsymbol{n}\right] \boldsymbol{n} \tag{1}$$

where $\boldsymbol{n}$ is the unit vector normal to $\mathcal{S}$ and $\boldsymbol{C}(\boldsymbol{\varepsilon}(t))$ is the homogenized constitutive tangent tensor. A macro-crack is nucleated at a point $\boldsymbol{x}_R$ when the condition:

$$\det(\boldsymbol{Q}) = 0 \tag{2}$$

is verified for the first time, t_N, in the loading history. The solution to this problem furnishes the triad $\{t_N, \boldsymbol{n}, \boldsymbol{\gamma}\}$, where $\boldsymbol{\gamma}$ is the initial velocity jump direction (see [1] for additional details). Once a cohesive crack has been nucleated, the point labeled $\boldsymbol{x}_R$ is re-labeled $\boldsymbol{x}_{\mathcal{S}}$ and the corresponding normal vector $\boldsymbol{n}$ remains fixed in time.

For a solid exhibiting displacement jumps (strong discontinuities) across $\mathcal{S}$, the total displacement vector, $\boldsymbol{u}$, can be described as follows [57]:

$$\boldsymbol{u} = \overbrace{\bar{\boldsymbol{u}}}^{\text{Continuous}} + \overbrace{\mathscr{M}\,\boldsymbol{\beta}}^{\text{Discontinuous}}, \quad \forall\, \boldsymbol{x} \in \Omega, \tag{3}$$

in terms of a continuous field, $\bar{\boldsymbol{u}}$, and a discontinuous contribution, $\mathscr{M}\,\boldsymbol{\beta}$. In (3), $\boldsymbol{\beta}$ is a smooth vector field in Ω, which is associated with the displacement discontinuity between the crack faces, while $\mathscr{M}$ is the unit jump function. Both, $\boldsymbol{\beta}$ and $\mathscr{M}$ are related to $\mathcal{S}$. The function $\mathscr{M}$ is defined as:

$$\mathscr{M} = \mathscr{H} - \varphi, \tag{4}$$

[3]Actually, multiple cohesive cracks can be nucleated at the macro-scale. In order to simplify the forthcoming equations, we assume the existence of a single cohesive macro-crack.

where $\mathscr{H}$ is the Heaviside step function shifted to $\mathcal{S}$ (see (5)-left) and φ is a sufficiently smooth and arbitrary function satisfying the two requirements shown in equation (5)-right. In (5), as well as in following expressions, some geometrical definitions are required: (i) $\mathcal{S}$ divides Ω into two sub-domains Ω_+ and Ω_- according to the $\boldsymbol{n}$-direction ($\boldsymbol{n}$ points towards Ω_+), see Fig. 2-(a), (ii) Ω^φ is an arbitrary small sub-domain of Ω including $\mathcal{S}$, with piecewise smooth boundary Γ^φ, see Fig. 2-(b), (iii) $\mathcal{S}$ divides Ω^φ into two sub-domains Ω^φ_+ and Ω^φ_- ($\boldsymbol{n}$ points towards Ω^φ_+). From equations (4)-(5) it is noted that $\mathscr{M}$ and $\boldsymbol{\beta}$ have compact support, where their support is Ω^φ.

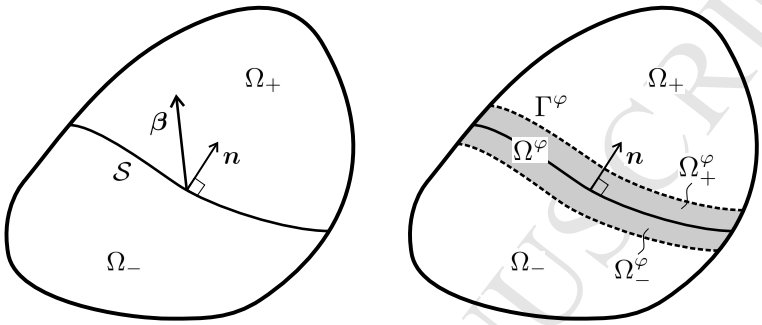

(a) (b)

Figure 2: Macro-mechanical problem exhibiting a strong discontinuity through the cohesive crack $\mathcal{S}$. Basic nomenclature to describe the kinematics.

The strain in $\boldsymbol{x}_R$ is:

$$\boldsymbol{\varepsilon}_R = \nabla^s_x \boldsymbol{u} = \nabla^s_x \bar{\boldsymbol{u}} + \mathscr{M} \nabla^s_x \boldsymbol{\beta} - \boldsymbol{\beta} \otimes^s \nabla_x \varphi, \quad \forall\, \boldsymbol{x}_R \in \Omega \backslash \mathcal{S}, \tag{6}$$

where $\nabla_x(\cdot)$ denotes the macro-scale gradient operator and the superscript $(\cdot)^s$ identifies the symmetric component of a tensor. Note that expression (6) contains only regular (bounded) terms and can be re-written as the sum of two contributions:

$$\boldsymbol{\varepsilon}_R = \boldsymbol{\varepsilon}_{\bar{\boldsymbol{u}}} + \boldsymbol{\varepsilon}_{\boldsymbol{\beta}}, \tag{7}$$

associated respectively with the continuous displacement field, $\bar{\boldsymbol{u}}$, and the jump discontinuity, $\boldsymbol{\beta}$:

$$\boldsymbol{\varepsilon}_{\bar{\boldsymbol{u}}} = \nabla^s_x \bar{\boldsymbol{u}}, \tag{8}$$

$$\boldsymbol{\varepsilon}_{\boldsymbol{\beta}} = \mathscr{M} \nabla^s_x \boldsymbol{\beta} - \boldsymbol{\beta} \otimes^s \nabla_x \varphi. \tag{9}$$

For points $\boldsymbol{x}_{\mathcal{S}}$ (at $\mathcal{S}$), we introduce the notion of generalized strain $\boldsymbol{\varepsilon}_{\mathcal{S}}$ characterized by the triad $\{\boldsymbol{\varepsilon}_R, \boldsymbol{\beta}, \boldsymbol{n}\}$ and composed by two independent entities:

$$\boldsymbol{\varepsilon}_{\mathcal{S}} = (\boldsymbol{\varepsilon}_R, \boldsymbol{\beta} \otimes^s \boldsymbol{n}), \tag{10}$$

where $(\boldsymbol{\beta} \otimes^s \boldsymbol{n})$ is related to a strong discontinuity at $\mathcal{S}$ whose normal vector is $\boldsymbol{n}$ and the crack opening is $\boldsymbol{\beta}$.

Next, we introduce the concept of kinematically admissible fields at the macro-scale. The total displacement $\boldsymbol{u}$, characterized by the pair $(\bar{\boldsymbol{u}}, \boldsymbol{\beta})$ (see equation (3)), is a kinematically admissible field if $\boldsymbol{u} \in \mathscr{U}$, where the set $\mathscr{U}$ is defined as

$$\mathscr{U} = \left\{ (\bar{\boldsymbol{u}}, \boldsymbol{\beta}) \,;\, \bar{\boldsymbol{u}} \in \boldsymbol{H}^1(\Omega) \,,\, \boldsymbol{\beta} \in \boldsymbol{H}^1(\Omega^\varphi) \text{ and } \bar{\boldsymbol{u}}|_{\Gamma_D} = \boldsymbol{u}_D \right\}. \tag{11}$$

From (11), virtual displacement actions, $\hat{\boldsymbol{u}}$, are kinematically admissible if $\hat{\boldsymbol{u}} \in \mathscr{V}$, with $\mathscr{V}$ the vector space defined as

$$\mathscr{V} = \left\{ (\hat{\bar{\boldsymbol{u}}}, \hat{\boldsymbol{\beta}}) \,;\, \hat{\bar{\boldsymbol{u}}} \in \boldsymbol{H}^1(\Omega) \,,\, \hat{\boldsymbol{\beta}} \in \boldsymbol{H}^1(\Omega^\varphi) \text{ and } \hat{\bar{\boldsymbol{u}}}|_{\Gamma_D} = \boldsymbol{0} \right\}, \tag{12}$$

where the superimposed hat, $\hat{(\cdot)}$, is used to denote kinematically admissible virtual actions.

All expressions presented in this section are valid for any time $t \in [0, \tau]$. In particular, for $t < t_N$ we have $\boldsymbol{\beta} \equiv \boldsymbol{0}$ (and also $\hat{\boldsymbol{\beta}} \equiv \boldsymbol{0}$) recovering a classical continuum kinematics.

For any time $t \in [0, \tau]$ and given prescribed values of external tractions $\boldsymbol{t}^e$ on Γ_N, find the kinematically admissible displacement fields $(\bar{\boldsymbol{u}}, \boldsymbol{\beta}) \in \mathscr{U}$, such that the stress state $\boldsymbol{\sigma}$ and the cohesive traction $\boldsymbol{T}$ satisfy the variational sentence:

$$\int_\Omega \boldsymbol{\sigma} \cdot \hat{\boldsymbol{\varepsilon}}_R \, d\Omega + \int_{\mathcal{S}} \boldsymbol{T} \cdot \hat{\boldsymbol{\beta}} \, d\mathcal{S} - \int_{\Gamma_N} \boldsymbol{t}^e \cdot \hat{\bar{\boldsymbol{u}}} \, d\Gamma = 0 \quad , \quad \forall \, (\hat{\bar{\boldsymbol{u}}}, \hat{\boldsymbol{\beta}}) \in \mathscr{V}. \tag{13}$$

Equation (13) is the Principle of Virtual Power (PVP) for solids exhibiting cohesive cracks. The product $\boldsymbol{T} \cdot \hat{\boldsymbol{\beta}}$ represents the internal virtual power contribution (per unit area) introduced by cohesive interfaces. For $t < t_N$ no cohesive tractions are included in the formulation.

2.4 Material response

In order to solve the variational problem (13), the macroscopic stress tensor $\boldsymbol{\sigma}$, as well as the cohesive traction $\boldsymbol{T}$, must be defined. For generic non-linear materials the corresponding constitutive functionals related to $\{\boldsymbol{\sigma}, \boldsymbol{T}\}$ can be symbolically expressed as follows:

$$\boldsymbol{\sigma} = \mathscr{F}(\boldsymbol{\varepsilon}_R^t) \quad , \quad \forall \, \boldsymbol{x}_R \in \Omega \backslash \mathcal{S} \, , \, \forall \, t \in [0, \tau], \tag{14}$$

$$\boldsymbol{T} = \mathscr{T}(\boldsymbol{\varepsilon}_R^t, \boldsymbol{\beta}^t) \quad , \quad \forall \, \boldsymbol{x}_{\mathcal{S}} \in \mathcal{S} \quad , \, \forall \, t \in [t_N, \tau], \tag{15}$$

where $(\cdot)^t$ denotes the history of the variable up to time t.

If the material and deformation processes under consideration are such that the complex interactions within the micro-structure cannot be easily captured by phenomenological laws, the characterization of $\{\mathscr{F}(\cdot), \mathscr{T}(\cdot)\}$ is usually an open problem. In this context, a multiscale formulation can be used as a general methodology to obtain the material behavior at the macro-scale, via homogenization of a micro-mechanical problem where all the inhomogeneities and their interactions are modeled by means of more fundamental mechanical laws. In the next section, a scale transition technique devised to provide the implicit form of $\{\mathscr{F}(\cdot), \mathscr{T}(\cdot)\}$ is proposed which completes the mechanical description of problem (13).

3 Multiscale formulation

The model considers two coupled scales of analysis. In what follows, a variational framework is taken, similar to that presented in [3, 30, 32, 55, 58, 59], which considers the mechanical interaction between macro and micro-scales for problems involving cohesive cracks at both levels of analysis.

This section describes the theoretical basis of this contribution. Special attention is focused on two topics: (I) to establish the minimum hypotheses required for defining the entire multiscale theory and (II) to derive the variational consequences of the model.

3.1 Preliminaries

Points at the micro-scale are denoted $\boldsymbol{y}$. The domain $\Omega_\mu \subset \mathbb{R}^{nd}$, identifies the heterogeneous RVE. The piecewise smooth boundary of Ω_μ is denoted Γ_μ, while $\boldsymbol{\nu}_\mu$ is the (outward) unit vector normal to Γ_μ, see Fig. 3-(a). Subscript $(\cdot)_\mu$ refers to any entity of the micro-scale domain.

Here we assume that multiple cohesive micro-cracks can be nucleated in the RVE for modeling strain localization phenomena and material degradation. Each crack is referred to as $\mathcal{S}_\mu^i$, with $i = 1, \ldots, n_c$, "n_c" being the total number of cohesive interfaces in the micro-scale. Micro-cracks can be either internal to the RVE-domain or intersect the RVE-boundary, see Fig. 3-(a). A criterion to nucleate a micro-crack needs to be specified. For example, we propose the detection of local material instabilities at each point $\boldsymbol{y}$, due to the singularity of the micro-scale localization tensor[4] $\boldsymbol{Q}_\mu$ [60–62]. Following this criterion, a micro-crack is nucleated at a point $\boldsymbol{y}$ when the condition:

[4]Here we are assuming that the underlying continuum constitutive relation that governs the bulk constitutive response before the micro-crack nucleation is based on softening-based evolution laws, so that local material instabilities can be induced (see Section 3.7.1).

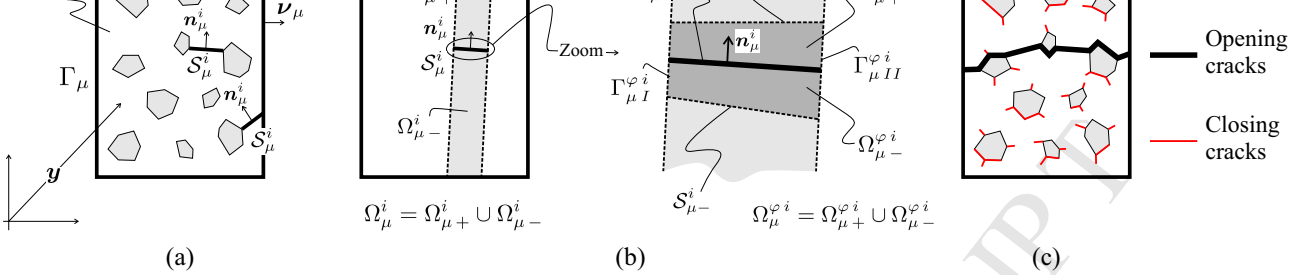

Figure 3: RVE with cohesive micro-cracks: (a) Internal crack and crack intersecting the RVE-boundary, (b) Nomenclature to describe strong discontinuities at the RVE, (c) Set of opening and closing micro-scale cohesive cracks at the nucleation time t_N.

$$\det(\boldsymbol{Q}_\mu) = 0, \quad \text{with} \quad \boldsymbol{Q}_\mu = \left[\boldsymbol{C}_\mu(\boldsymbol{\varepsilon}_\mu)\, \boldsymbol{n}_\mu\right] \boldsymbol{n}_\mu, \tag{16}$$

is satisfied for the first time in the loading history, $\boldsymbol{\varepsilon}_\mu$ being the strain tensor at the micro-scale. The solution to this problem provides the triad $\{t^i_{N\mu}, \boldsymbol{n}^i_\mu, \boldsymbol{\gamma}^i_\mu\}$, where $t^i_{N\mu} \in [0, \tau]$ is the crack nucleation time, $\boldsymbol{n}^i_\mu$ is the unit normal vector and $\boldsymbol{\gamma}^i_\mu$ represents the initial jump rate; all related to the specific cohesive micro-crack $\mathcal{S}^i_\mu$.

Remark 3.1 *The model can also deal with pre-existing traction-free or adhesive interfaces, see for example [48, 50, 63]. In the present framework, adhesive interfaces are a particular class of cohesive cracks, equipped with a specific constitutive law being nucleated from the beginning of the analysis ($t^i_{A\mu} = 0$).*

3.2 Kinematical assumptions in the scale transition (H1)

In this section we introduce the first hypothesis H1 of the proposed formulation. It is convenient to write the kinematics in incremental form. Thus, the operator $d(\cdot)$ is used to denote incremental quantities.

3.2.1 Micro-scale kinematics

Following the ideas developed in [1–3, 55], the increment of the strain field at the micro-scale, $d\boldsymbol{\varepsilon}_\mu$, can be defined in terms of: (i) the insertion of the relevant macro-scale kinematics ($\{d\boldsymbol{\varepsilon}_{\bar{\boldsymbol{u}}}, d\boldsymbol{\varepsilon}_{\boldsymbol{\beta}}, d\boldsymbol{\beta}\}$) into the micro-scale, by means of a specific Insertion Operator $\boldsymbol{\mathcal{I}}(\cdot)$, and (ii) a fluctuation component,

$$d\boldsymbol{\varepsilon}_\mu = \boldsymbol{\mathcal{I}}(d\boldsymbol{\varepsilon}_{\bar{\boldsymbol{u}}}, d\boldsymbol{\varepsilon}_{\boldsymbol{\beta}}, d\boldsymbol{\beta}) + d\tilde{\boldsymbol{\varepsilon}}_\mu, \quad \forall\, \boldsymbol{y} \in \Omega_\mu, \tag{17}$$

Terms $\boldsymbol{\mathcal{I}}(\cdot)$ and $d\tilde{\boldsymbol{\varepsilon}}_\mu$ in equation (17), are discussed in detail in the following. The notation $\tilde{(\cdot)}$ will be used to refer to any fluctuation field at the micro-scale.

Fluctuation fields

Displacement discontinuities in the micro-scale domain are treated in an analogous way to that introduced in Section 2.2. Hence, the (incremental) micro-scale displacement fluctuation, $d\tilde{\boldsymbol{u}}_\mu$, can be defined as

$$d\tilde{\boldsymbol{u}}_\mu = \overbrace{d\tilde{\bar{\boldsymbol{u}}}_\mu}^{\text{Continuous}} + \overbrace{\sum_{i=1}^{n_c} \mathscr{M}^i_\mu\, d\tilde{\boldsymbol{\beta}}^i_\mu}^{\text{Discontinuous}}, \quad \forall\, \boldsymbol{y} \in \Omega_\mu, \tag{18}$$

with $d\tilde{\bar{\boldsymbol{u}}}_\mu$ the (incremental) regular part of the displacement fluctuation, $\mathscr{M}^i_\mu$ the unit jump function and $d\tilde{\boldsymbol{\beta}}^i_\mu$ the (incremental) fluctuation of the opening crack displacement. Both, $\mathscr{M}^i_\mu$ and $d\tilde{\boldsymbol{\beta}}^i_\mu$, are defined for each micro-scale cohesive crack labeled "i". In view of (18), consider that the set of independent kinematical descriptors

$$\mathscr{M}_\mu^i := \mathscr{H}_\mu^i - \varphi_\mu^i, \tag{19}$$

$$\mathscr{H}_\mu^i = \begin{cases} 0 & \forall\, \boldsymbol{y} \in \Omega_{\mu-}^i \\ 1 & \forall\, \boldsymbol{y} \in \Omega_{\mu+}^i \end{cases}, \quad \varphi_\mu^i = \begin{cases} 0 & \forall\, \boldsymbol{y} \in \Omega_{\mu-}^i \backslash \Omega_{\mu-}^{\varphi\, i} \\ 1 & \forall\, \boldsymbol{y} \in \Omega_{\mu+}^i \backslash \Omega_{\mu+}^{\varphi\, i} \end{cases}, \tag{20}$$

where the geometrical interpretations for the domains Ω_μ^i, $\Omega_{\mu+}^i$, $\Omega_{\mu-}^i$, $\Omega_\mu^{\varphi\, i}$, $\Omega_{\mu+}^{\varphi\, i}$ and $\Omega_{\mu-}^{\varphi\, i}$ are depicted in Fig. 3-(b). Note that $\mathscr{M}_\mu^i$ has the compact support $\Omega_\mu^{\varphi\, i}$.

The (incremental) micro-scale strain fluctuation term, $d\tilde{\boldsymbol{\varepsilon}}_\mu$, can be evaluated by applying the generalized symmetric gradient operator to $d\tilde{\boldsymbol{u}}_\mu$, yielding:

$$d\tilde{\boldsymbol{\varepsilon}}_\mu = d\tilde{\boldsymbol{\varepsilon}}_{\mu R} + \sum_{i=1}^{n_c} \left(d\tilde{\boldsymbol{\beta}}_\mu^i \otimes^s \boldsymbol{n}_\mu^i\right) \delta_\mu^i, \quad \forall\, \boldsymbol{y} \in \Omega_\mu, \tag{21}$$

with $d\tilde{\boldsymbol{\varepsilon}}_{\mu R}$ being the incremental regular (bounded) micro-scale strain fluctuation field defined as:

$$d\tilde{\boldsymbol{\varepsilon}}_{\mu R} = \nabla_y^s\, d\tilde{\boldsymbol{u}}_\mu + \sum_{i=1}^{n_c} \left[\mathscr{M}_\mu^i \nabla_y^s\, d\tilde{\boldsymbol{\beta}}_\mu^i - d\tilde{\boldsymbol{\beta}}_\mu^i \otimes^s \nabla_y \varphi_\mu^i\right], \quad \forall\, \boldsymbol{y} \in \Omega_\mu \backslash (\cup_{i=1}^{n_c} \mathcal{S}_\mu^i), \tag{22}$$

where $\nabla_y(\cdot)$ represents the micro-scale gradient operator and δ_μ^i (with unit of $[\text{length}]^{-1}$) is the Dirac distribution shifted to $\mathcal{S}_\mu^i$. Note the similar structure shared by $d\tilde{\boldsymbol{\varepsilon}}_{\mu R}$ and its macro-scale counterpart $\boldsymbol{\varepsilon}_R$, presented in (6).

For convenience, we shall explore the fact that the kinematical description of each micro-crack is equivalent to the kinematics of a strain localization band whose thickness, ℓ_μ, tends to zero. Thus, the length parameter ℓ_μ^i, associated with each micro-crack "i", is included in the expressions that follow. This is not a strictly required assumption, but a convenient way to deal with micro-cracks[5]. Accordingly, expression (21) can be re-written as the limit case of strain localization bands in sub-domains $\Omega_{\mathcal{S}_\mu^i}$ ($\Omega_{\mathcal{S}_\mu^i}$ includes $\mathcal{S}_\mu^i$) of thickness ℓ_μ^i, when $\ell_\mu^i \to 0$ (see Appendix I-(a) for additional details on the limiting process from a continuous strain localization-based kinematics to a discontinuous kinematics):

$$d\tilde{\boldsymbol{\varepsilon}}_\mu = \overbrace{d\tilde{\boldsymbol{\varepsilon}}_{\mu R}}^{\text{Regular term}} + \overbrace{\sum_{i=1}^{n_c} \lim_{\ell_\mu^i \to 0} \phi_\mu^i\, \frac{d\tilde{\boldsymbol{\beta}}_\mu^i \otimes^s \boldsymbol{n}_\mu^i}{\ell_\mu^i}}^{\text{Singular terms}}, \quad \forall\, \boldsymbol{y} \in \Omega_\mu, \tag{23}$$

$$\phi_\mu^i = \begin{cases} 1 & \forall\, \boldsymbol{y} \in \Omega_{\mathcal{S}_\mu^i} \\ 0 & \text{otherwise,} \end{cases} \tag{24}$$

with ϕ_μ^i a collocation function related to the sub-domain $\Omega_{\mathcal{S}_\mu^i} \subset \Omega_\mu^{\varphi\, i}$, defined for each $\mathcal{S}_\mu^i$. Roughly speaking, $\Omega_{\mathcal{S}_\mu^i}$ identifies each sub-domain where strain localization happens by the elements $\{\mathcal{S}_\mu^i, \ell_\mu^i\}$, where $\mathcal{S}_\mu^i$ is the mean surface of $\Omega_{\mathcal{S}_\mu^i}$ and ℓ_μ^i is the thickness of the localization band (see Fig. 22-(a) in Appendix I-(a)).

The set of equations (18)-(24) completely defines the micro-scale kinematics related to fluctuation fields.

Insertion procedure, $\boldsymbol{\mathcal{I}}(\cdot)$

By *"insertion procedure"* we mean the form in which macro-scale kinematical information is transferred into the micro-scale domain. In the present context, it establishes how the incremental point-valued quantities $\{d\boldsymbol{\varepsilon}_{\bar{\boldsymbol{u}}}, d\boldsymbol{\varepsilon}_{\boldsymbol{\beta}}, d\boldsymbol{\beta}\}$, at $\boldsymbol{x}$, are inserted into the RVE domain. We denote the (linear) insertion operator as $\boldsymbol{\mathcal{I}}(d\boldsymbol{\varepsilon}_{\bar{\boldsymbol{u}}}, d\boldsymbol{\varepsilon}_{\boldsymbol{\beta}}, d\boldsymbol{\beta})$. The main degree of arbitrariness in postulating multiscale models of the present type lies in the definition of the insertion mechanism.

Before defining the $\boldsymbol{\mathcal{I}}(\cdot)$-operator, some important mechanical aspects need to be considered:

[5]For example, by considering cracks as strain localization bands of finite thickness, we can deal with finite localization bands as well as cohesive cracks in the micro-scale domain, simultaneously, in an unified kinematical framework. The locally variable parameter $\ell_\mu^i(\boldsymbol{y})$ defines the kinematical character of each point in the failure zone of the RVE: $\ell_\mu^i(\boldsymbol{y}) \to 0$ means a crack, $\ell_\mu^i(\boldsymbol{y}) \neq 0$ means a localization band. There are additional benefits in adopting this type of kinematical representation for micro-cracks, which will be highlighted later.

The opening micro-crack set determines the evolving RVE failure mechanism at $t = t_N$, which governs (in an average sense) the evolution of the macro-scale cohesive crack. It is denoted $\mathcal{S}_\mu^L$ and defined as $\mathcal{S}_\mu^L = \bigcup_{j=1}^{n_{op}} \mathcal{S}_\mu^{Lj}$ $(j = 1, \ldots, n_{op})$, where "n_{op}" is the total number of opening micro-cracks, at $t = t_N$. Thus, we are assuming that $\mathcal{S}_\mu^L$ is a possible tortuous connected/disconnected piecewise poly-interface composed of several interfaces, each representing an opening micro-crack $\mathcal{S}_\mu^{Lj}$. A criterion to determine $\mathcal{S}_\mu^L$ at $t = t_N$ is explained in Appendix I-(b).

Alternatively, closing micro-cracks in the RVE are cohesive interfaces that have been nucleated during the stable period of the material at the macro-scale, i.e. during the interval $t \in [0, t_N]$. However, due to the loading-unloading effect triggered by the strain localization process at the RVE-domain, they close onward. This concept will be further clarified when the methodology to determine $\mathcal{S}_\mu^L$ is discussed in Appendix I-(b).

From now on, superscript "L" is added to all entities related to the domain $\mathcal{S}_\mu^L$. Superscript "j" is used to denote objects associated to a particular opening micro-crack $\mathcal{S}_\mu^{Lj} \subset \mathcal{S}_\mu^L$, while the superscript "i" is used to identify any micro-crack in the RVE (opening or closing).

(b) Expressions (9) and (10) for the macro-scale kinematical descriptors $\{\boldsymbol{\varepsilon}_{\boldsymbol{\beta}}, \boldsymbol{\varepsilon}_{\mathcal{S}}\}$, to be inserted into the RVE, have a mechanical meaning within a single-scale setting. They are built on the basis that the unit-jump function, $\mathscr{M}$, is univocally determined once the unit vector $\boldsymbol{n}$ is given at point $\boldsymbol{x}_{\mathcal{S}} \in \mathcal{S}$ (see equations (3) and (4)). Considering the RVE connected to the point $\boldsymbol{x}_{\mathcal{S}}$, the failure crack path is intricate and composed of several, not necessary aligned, micro-cracks. Thus, expressions (9) and (10) are no longer entirely consistent with the kinematics of the RVE. It is expected that the macro-scale normal vector $\boldsymbol{n}$ is related to some averaged quantity of the spatially variable unit normal vector field at the micro-scale $\boldsymbol{n}_\mu^{Lj}$, $j = 1, \ldots, n_{op}$ (the set of vectors being normal to the opening micro-scale cohesive cracks at $t = t_N$). However the averaging of unit vectors $\boldsymbol{n}_\mu^{Lj}$ with arbitrary orientations does not result in a unit vector. This fact suggests that a proper scaling factor must be taken into account to make the macro-scale terms containing the jump $\boldsymbol{\beta}$ (i.e. $\boldsymbol{\varepsilon}_{\boldsymbol{\beta}}$ and $\boldsymbol{\varepsilon}_{\mathcal{S}}$) compatible with the micro-scale kinematical description showing a zig-zag crack path. A postulate in the present formulation is that this scaling factor, called *tortuosity* index and denoted θ, is incorporated in the definition of the $\boldsymbol{\mathcal{I}}(\cdot)$-operator, specifically in the $\boldsymbol{\mathcal{I}}(\mathbf{0}, d\boldsymbol{\varepsilon}_{\boldsymbol{\beta}}, d\boldsymbol{\beta})$-counterpart of the insertion operator.

Taking into account items (a) and (b) above, we are in a position to postulate the insertion procedure, according to expression (17). The insertion operator, $\boldsymbol{\mathcal{I}}(d\boldsymbol{\varepsilon}_{\bar{\boldsymbol{u}}}, d\boldsymbol{\varepsilon}_{\boldsymbol{\beta}}, d\boldsymbol{\beta})$, is defined through the following rules:

- The increment of regular macro-scale strain, $d\boldsymbol{\varepsilon}_R = d\boldsymbol{\varepsilon}_{\bar{\boldsymbol{u}}} + d\boldsymbol{\varepsilon}_{\boldsymbol{\beta}}$, given by equations (7), (9) and (10), is uniformly inserted throughout the micro-scale domain Ω_μ. This insertion mechanism is symbolically expressed as $\boldsymbol{\mathcal{I}}(d\boldsymbol{\varepsilon}_{\bar{\boldsymbol{u}}}, d\boldsymbol{\varepsilon}_{\boldsymbol{\beta}}, \mathbf{0})$.

- The increment of the macro-scale displacement jump $d\boldsymbol{\beta}$ is only inserted where the generalized fluctuation strain field $(d\tilde{\boldsymbol{\varepsilon}}_\mu)$ localizes in the RVE-domain. In this case, throughout the domain $\mathcal{S}_\mu^L$ of all opening micro-cracks[6]. This insertion mechanism is symbolically expressed as $\boldsymbol{\mathcal{I}}(\mathbf{0}, \mathbf{0}, d\boldsymbol{\beta})$.

Accordingly (see Fig. 4), $\boldsymbol{\mathcal{I}}(\cdot)$ can be defined as:

$$\boldsymbol{\mathcal{I}}_R(d\boldsymbol{\varepsilon}_{\bar{\boldsymbol{u}}}, d\boldsymbol{\varepsilon}_{\boldsymbol{\beta}}) := \boldsymbol{\mathcal{I}}(d\boldsymbol{\varepsilon}_{\bar{\boldsymbol{u}}}, \mathbf{0}, \mathbf{0}) + \boldsymbol{\mathcal{I}}(\mathbf{0}, d\boldsymbol{\varepsilon}_{\boldsymbol{\beta}}, \mathbf{0}) = \underbrace{\overbrace{d\boldsymbol{\varepsilon}_{\bar{\boldsymbol{u}}} + \theta\, d\boldsymbol{\varepsilon}_{\boldsymbol{\beta}}}^{\boldsymbol{\mathcal{I}}(d\boldsymbol{\varepsilon}_{\bar{\boldsymbol{u}}}, d\boldsymbol{\varepsilon}_{\boldsymbol{\beta}}, \mathbf{0})}}_{\text{Uniform insertion of } d\boldsymbol{\varepsilon}_R} \quad , \quad \forall\, \boldsymbol{y} \in \Omega_\mu, \text{ for } \boldsymbol{x}_R, \tag{25}$$

$$\boldsymbol{\mathcal{I}}_{\mathcal{S}}(d\boldsymbol{\varepsilon}_{\bar{\boldsymbol{u}}}, d\boldsymbol{\varepsilon}_{\boldsymbol{\beta}}, d\boldsymbol{\beta}) := \underbrace{\overbrace{d\boldsymbol{\varepsilon}_{\bar{\boldsymbol{u}}} + \theta\, d\boldsymbol{\varepsilon}_{\boldsymbol{\beta}}}^{\boldsymbol{\mathcal{I}}(d\boldsymbol{\varepsilon}_{\bar{\boldsymbol{u}}}, d\boldsymbol{\varepsilon}_{\boldsymbol{\beta}}, \mathbf{0})}}_{\text{Uniform insertion of } d\boldsymbol{\varepsilon}_R} + \underbrace{\overbrace{\sum_{j=1}^{n_{op}} \left[\lim_{\ell_\mu^{Lj} \to 0} \phi_\mu^{Lj} \frac{\theta\, d\boldsymbol{\beta} \otimes^s \boldsymbol{n}_\mu^{Lj}}{\ell_\mu^{Lj}} \right]}^{\boldsymbol{\mathcal{I}}(\mathbf{0}, \mathbf{0}, d\boldsymbol{\beta})}}_{\text{Localized insertion of } d\boldsymbol{\beta}}, \quad \forall\, \boldsymbol{y} \in \Omega_\mu, \text{ for } \boldsymbol{x}_{\mathcal{S}}, \tag{26}$$

[6]Recall that $\mathcal{S}_\mu^L$ is idealized as a sub-domain containing all strain localization bands $\Omega_{\mathcal{S}_\mu^i}$ whose thicknesses approach zero, at the macro-scale nucleation time t_N

$\boldsymbol{x}_R$ and $\boldsymbol{x}_{\mathcal{S}}$, respectively. From (25) and (26), it is clear that the localized insertion of $d\boldsymbol{\beta}$ into the RVE (given by $\boldsymbol{\mathcal{I}}(\mathbf{0},\mathbf{0},d\boldsymbol{\beta})$), makes sense only for points $\boldsymbol{x}_{\mathcal{S}}$ located on the cohesive macro-crack.

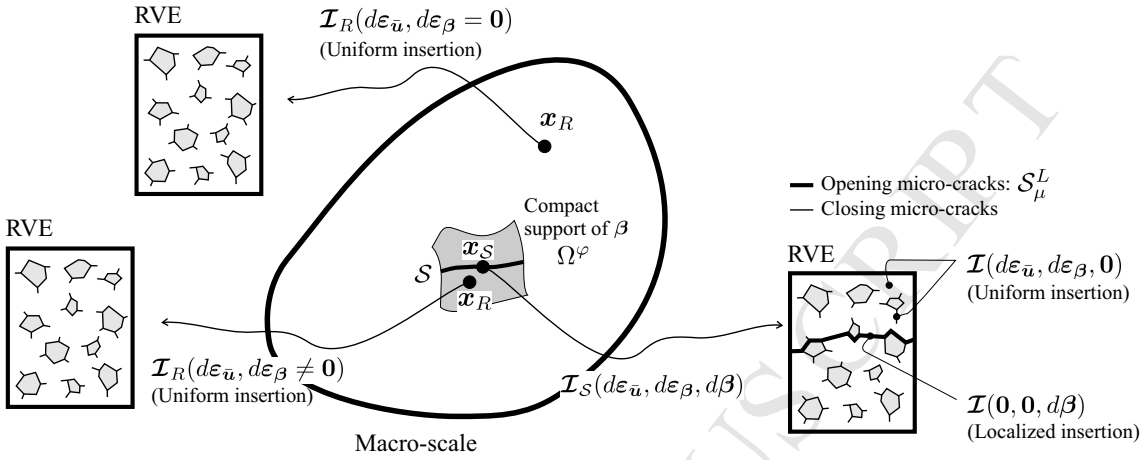

Figure 4: Insertion procedure for points $\boldsymbol{x}_R$ and $\boldsymbol{x}_{\mathcal{S}}$.

Remark 3.2 *All the $\boldsymbol{\mathcal{I}}(\cdot)$-terms, i.e. $\boldsymbol{\mathcal{I}}(d\boldsymbol{\varepsilon}_{\bar{\boldsymbol{u}}},\mathbf{0},\mathbf{0})$, $\boldsymbol{\mathcal{I}}(\mathbf{0},d\boldsymbol{\varepsilon}_{\boldsymbol{\beta}},\mathbf{0})$ and $\boldsymbol{\mathcal{I}}(\mathbf{0},\mathbf{0},d\boldsymbol{\beta})$, are linear operators.*

Recall that the θ-factor considered in the insertion of $d\boldsymbol{\varepsilon}_{\boldsymbol{\beta}}$ and $d\boldsymbol{\beta}$ (see expressions (25) and (26)), takes into account the possibly tortuous path of $\mathcal{S}_\mu^L$, in a homogenized sense. The tortuosity parameter θ is defined as follows:

$$\theta = \frac{|\mathcal{S}_\mu^L|}{\Big|\sum_{j=1}^{n_{op}} \int_{\mathcal{S}_\mu^{Lj}} \boldsymbol{n}_\mu^{Lj}\, d\mathcal{S}_\mu\Big|}, \quad |\mathcal{S}_\mu^L| = \sum_{j=1}^{n_{op}} |\mathcal{S}_\mu^{Lj}|, \tag{27}$$

and represents an average weighing factor due to possibly misaligned normal unit vectors $\boldsymbol{n}_\mu^{Lj}$ along the path of opening cohesive cracks at the micro-scale. This tortuosity parameter (which is the inverse of the scalar index introduced by the authors in [3]) is related to the nucleation of the macro-scale kinematical descriptor $d\boldsymbol{\beta}$. Thus, it has to be computed at the macro-scale nucleation time $t = t_N$, looking for the failure zone in the corresponding RVE. Appendix I-(c) justifies the tortuosity factor definition through a purely kinematical condition fulfilled by the insertion operator $\boldsymbol{\mathcal{I}}(\cdot)$. Observe that in the particular case of uniformly oriented opening micro-cracks (i.e. all the normal vectors $\boldsymbol{n}_\mu^{Lj}$ are co-linear), the tortuosity index results $\theta = 1$. As the failure path in the RVE becomes more tortuous, the θ-index increases, so we have $\theta \in [1, \infty)$.

Collecting the expressions (25)-(26) and (23), the (incremental) micro-scale strain fluctuation field $d\boldsymbol{\varepsilon}_\mu$ (see (17)) yields:

$$d\boldsymbol{\varepsilon}_\mu = \overbrace{d\boldsymbol{\varepsilon}_{\bar{\boldsymbol{u}}} + \theta\, d\boldsymbol{\varepsilon}_{\boldsymbol{\beta}}}^{\boldsymbol{\mathcal{I}}_R(\cdot)} + \overbrace{d\tilde{\boldsymbol{\varepsilon}}_{\mu R} + \sum_{i=1}^{n_c} \Big[\lim_{\ell_\mu^i \to 0} \phi_\mu^i\, \frac{d\tilde{\boldsymbol{\beta}}_\mu^i \otimes^s \boldsymbol{n}_\mu^i}{\ell_\mu^i} \Big]}^{d\tilde{\boldsymbol{\varepsilon}}_\mu}, \qquad \forall\, \boldsymbol{y}, \quad \text{for } \boldsymbol{x}_R, \tag{28}$$

and

$$d\boldsymbol{\varepsilon}_\mu = \overbrace{d\boldsymbol{\varepsilon}_{\bar{\boldsymbol{u}}} + \theta\, d\boldsymbol{\varepsilon}_{\boldsymbol{\beta}} + \sum_{j=1}^{n_{op}} \Big[\lim_{\ell_\mu^{Lj} \to 0} \phi_\mu^{Lj}\, \frac{\theta\, d\boldsymbol{\beta} \otimes^s \boldsymbol{n}_\mu^{Lj}}{\ell_\mu^{Lj}} \Big] + \underbrace{d\tilde{\boldsymbol{\varepsilon}}_{\mu R} + \sum_{i=1}^{n_c} \Big[\lim_{\ell_\mu^i \to 0} \phi_\mu^i\, \frac{d\tilde{\boldsymbol{\beta}}_\mu^i \otimes^s \boldsymbol{n}_\mu^i}{\ell_\mu^i} \Big]}_{d\tilde{\boldsymbol{\varepsilon}}_\mu}}^{\boldsymbol{\mathcal{I}}_{\mathcal{S}}(\cdot)}, \qquad \forall \boldsymbol{y}, \quad \text{for } \boldsymbol{x}_{\mathcal{S}}. \tag{29}$$

$$d\boldsymbol{\beta}_{\mu}^{Lj} = \theta\, d\boldsymbol{\beta} + d\tilde{\boldsymbol{\beta}}_{\mu}^{Lj}, \quad j = 1, \ldots, n_{op}. \tag{30}$$

The kinematical description at the RVE is fully defined by expressions (17)-(29).

3.2.2 Kinematical Admissibility requirement in the RVE

Additional "*Kinematical Admissibility*" requirements must be introduced in order to fully connect the kinematics at macro and micro-scales. This is a key issue in multiscale modeling in general and constitutes, together with the insertion operator definition, the main ingredients of the first hypothesis (H1).

Here we postulate that the increment of micro-scale strains $d\boldsymbol{\varepsilon}_{\mu}$, in the RVE related to $\boldsymbol{x}_R$, is a kinematically admissible field with respect to the macro-scale quantities $d\boldsymbol{\varepsilon}_{\bar{\boldsymbol{u}}}$ and $d\boldsymbol{\varepsilon}_{\boldsymbol{\beta}}$, if it satisfies the following constraint:

$$\int_{\Omega_{\mu}} \boldsymbol{\mathcal{I}}_R(d\boldsymbol{\varepsilon}_{\bar{\boldsymbol{u}}}, d\boldsymbol{\varepsilon}_{\boldsymbol{\beta}})\, d\Omega_{\mu} = \int_{\Omega_{\mu}} d\boldsymbol{\varepsilon}_{\mu}\, d\Omega_{\mu}. \tag{31}$$

Further, we postulate that the incremental micro-scale strain $d\boldsymbol{\varepsilon}_{\mu}$, in the RVE related to $\boldsymbol{x}_{\mathcal{S}}$, is a kinematically admissible field with respect to the macro-scale quantities $d\boldsymbol{\varepsilon}_{\bar{\boldsymbol{u}}}$, $d\boldsymbol{\varepsilon}_{\boldsymbol{\beta}}$ and $d\boldsymbol{\beta}$, if it satisfies both (31) and the following additional constraint:

$$\int_{\Omega_{\mu}^{L}} \boldsymbol{\mathcal{I}}_{\mathcal{S}}(d\boldsymbol{\varepsilon}_{\bar{\boldsymbol{u}}}, d\boldsymbol{\varepsilon}_{\boldsymbol{\beta}}, d\boldsymbol{\beta})\, d\Omega_{\mu} = \int_{\Omega_{\mu}^{L}} d\boldsymbol{\varepsilon}_{\mu}\, d\Omega_{\mu}, \tag{32}$$

where $\Omega_{\mu}^{L} = \bigcup_{j=1}^{n_{op}} \Omega_{\mathcal{S}_{\mu}^{Lj}}$ is the total strain localization domain in the RVE.

Expressions (31)-(32) imply that the micro-scale strain fluctuation field, $d\tilde{\boldsymbol{\varepsilon}}_{\mu}$, satisfies:

- zero integral value over the domain Ω_{μ}, for an RVE linked to a regular point $\boldsymbol{x}_R$, and
- zero integral value over the domains Ω_{μ} and Ω_{μ}^{L}, for an RVE linked to a singular point $\boldsymbol{x}_{\mathcal{S}}$.

Thus, the constraints (31)-(32) ensure that the fluctuation field, $d\tilde{\boldsymbol{\varepsilon}}_{\mu}$, does not contribute to the macro-scale kinematics, given by the descriptors $\{d\boldsymbol{\varepsilon}_{\bar{\boldsymbol{u}}}, d\boldsymbol{\varepsilon}_{\boldsymbol{\beta}}, d\boldsymbol{\beta}\}$ valued at $\boldsymbol{x}$.

Remark 3.3 *The kinematical admissibility requirements,* (31) *and* (32)*, have been written using the same format as in previous contributions by the authors (see [1, 2]). This is a direct consequence of the adopted kinematical representation for cracks at the micro-scale, considered as the limit case of strain localization bands. Note that the singular terms related to displacement discontinuities in the RVE are included in the definition of* $d\boldsymbol{\varepsilon}_{\mu}$ *(see* (28)-(29)*).*

From the definitions (25) and (28), equation (31) yields:

$$\int_{\Omega_{\mu}} d\tilde{\boldsymbol{\varepsilon}}_{\mu R} + \sum_{i=1}^{n_c} \left[\lim_{\ell_{\mu}^{i} \to 0} \phi_{\mu}^{i}\, \frac{d\tilde{\boldsymbol{\beta}}_{\mu}^{i} \otimes^{s} \boldsymbol{n}_{\mu}^{i}}{\ell_{\mu}^{i}} \right] d\Omega_{\mu} = \boldsymbol{0}, \tag{33}$$

which, after mathematical manipulations (see details in Appendix II-(b)), reduces to:

$$\int_{\Omega_{\mu}} \nabla_{y}^{s}\, d\tilde{\boldsymbol{u}}_{\mu}\, d\Omega_{\mu} = \int_{\Gamma_{\mu}} d\tilde{\boldsymbol{u}}_{\mu} \otimes^{s} \boldsymbol{\nu}_{\mu}\, d\Gamma_{\mu} = \boldsymbol{0}, \tag{34}$$

Observe that the first admissibility requirement, given by expression (31) or (34), results in the standard minimal kinematical constraint imposed on the (increment of) regular micro-scale displacement fluctuations at the RVE-boundary Γ_{μ}, see [1, 3, 32, 55, 58] for more details on this standard issue. Thus, the term Standard Boundary Condition (SBC) is used to denote it. Also note, in (34), that no constraints appear on the micro-scale displacement fluctuation jump $d\tilde{\boldsymbol{\beta}}_{\mu}^{i}$.

In turn, from (26) and (29), expression (32) can be re-written as:

which simplifies to:

$$\sum_{j=1}^{n_{op}} \int_{\mathcal{S}_\mu^{Lj}} d\tilde{\boldsymbol{\beta}}_\mu^{Lj} \otimes^s \boldsymbol{n}_\mu^{Lj}\, d\mathcal{S}_\mu = \boldsymbol{0}. \tag{36}$$

Equation (36) is an additional constraint on the (increment of) micro-scale displacement fluctuation jump across $\mathcal{S}_\mu^L$, for an RVE linked to $\boldsymbol{x}_\mathcal{S}$. The term Non-Standard Boundary Condition (NSBC) refers to the kinematical constraint given in (36). It does not involve the regular counterpart of the (incremental) displacement fluctuation $d\tilde{\boldsymbol{u}}_\mu$. Thus, (34) and (36) are uncoupled linear constraints.

In view of (34) and (36), we say that $d\tilde{\boldsymbol{u}}_\mu$ is kinematically admissible if $d\tilde{\boldsymbol{u}}_\mu \in \tilde{\mathscr{U}}_\mu^R$ for an RVE linked to a point $\boldsymbol{x}_R$, or $d\tilde{\boldsymbol{u}}_\mu \in \tilde{\mathscr{U}}_\mu^\mathcal{S}$ for an RVE linked to a point $\boldsymbol{x}_\mathcal{S}$, where:

$$\tilde{\mathscr{U}}_\mu^R = \Big\{ (d\tilde{\boldsymbol{u}}_\mu, d\tilde{\boldsymbol{\beta}}_\mu^1, \ldots, d\tilde{\boldsymbol{\beta}}_\mu^{n_c}) \,;\; d\tilde{\boldsymbol{u}}_\mu \in \boldsymbol{H}^1(\Omega_\mu) \,,\; d\tilde{\boldsymbol{\beta}}_\mu^i \in \boldsymbol{H}^1(\Omega_\mu^{\varphi\, i}),\; i = 1, \ldots, n_c, \text{ such that } \int_{\Gamma_\mu} d\tilde{\boldsymbol{u}}_\mu \otimes^s \boldsymbol{\nu}_\mu\, d\Gamma_\mu = \boldsymbol{0} \Big\}. \tag{37}$$

and

$$\tilde{\mathscr{U}}_\mu^\mathcal{S} = \Big\{ (d\tilde{\boldsymbol{u}}_\mu, d\tilde{\boldsymbol{\beta}}_\mu^1, \ldots, d\tilde{\boldsymbol{\beta}}_\mu^{n_c}) \,;\; d\tilde{\boldsymbol{u}}_\mu \in \boldsymbol{H}^1(\Omega_\mu) \,,\; d\tilde{\boldsymbol{\beta}}_\mu^i \in \boldsymbol{H}^1(\Omega_\mu^{\varphi\, i}),\; i = 1, \ldots, n_c, \text{ such that } \int_{\Gamma_\mu} d\tilde{\boldsymbol{u}}_\mu \otimes^s \boldsymbol{\nu}_\mu\, d\Gamma_\mu = \boldsymbol{0} \;\text{ and }\; \sum_{j=1}^{n_{op}} \int_{\mathcal{S}_\mu^{Lj}} d\tilde{\boldsymbol{\beta}}_\mu^{Lj} \otimes^s \boldsymbol{n}_\mu^{Lj} = \boldsymbol{0} \Big\}. \tag{38}$$

At points $\boldsymbol{x}_R$, virtual actions of micro-scale displacement fluctuations, $\hat{\boldsymbol{u}}_\mu$, are kinematically admissible if $\hat{\boldsymbol{u}}_\mu \in \mathscr{V}_\mu^R \equiv \tilde{\mathscr{U}}_\mu^R$. Alternatively, at points $\boldsymbol{x}_\mathcal{S}$, virtual actions are kinematically admissible if $\hat{\boldsymbol{u}}_\mu \in \mathscr{V}_\mu^\mathcal{S} \equiv \tilde{\mathscr{U}}_\mu^\mathcal{S}$.

Remark 3.4 *Considering problems involving cohesive cracks at both scales of analysis, the vector spaces $\tilde{\mathscr{U}}_\mu^R$ ($\equiv \mathscr{V}_\mu^R$) and $\tilde{\mathscr{U}}_\mu^\mathcal{S}$ ($\equiv \mathscr{V}_\mu^\mathcal{S}$), defined by* (37) *and* (38) *respectively, characterize the so-called multiscale model with minimum kinematical constraints. More kinematically constrained multiscale sub-models can be derived by taking sub-spaces of $\tilde{\mathscr{U}}_\mu^R$ or $\tilde{\mathscr{U}}_\mu^\mathcal{S}$. In Section 5, some examples of different multiscale sub-models are presented.*

3.3 Principle of Multiscale Virtual Power (H2)

So far, only kinematical constraints have been considered in the macro-to-micro information transfer. Physical consistency of the multiscale model is achieved by balancing, in addition, the internal virtual power at both scales. For this purpose, an adapted version of the Hill-Mandel principle [21, 54] is introduced, which accounts for cohesive cracks at the macro and micro-scales (the second fundamental hypothesis of our approach (H2)). To achieve this objective, the notion of *virtual kinematically admissible macro-scale generalized strain actions* to be considered in the macro-to-micro scale transfer ($\hat{\boldsymbol{\varepsilon}}_R$ and $\hat{\boldsymbol{\beta}}$), must be defined. These definitions depend on the mechanical regime at the macro-scale. In this sense, we postulate that kinematically admissible macro-scale virtual strains actions are:

$$\hat{\boldsymbol{\beta}} \equiv \boldsymbol{0} \qquad \text{and} \qquad \hat{\boldsymbol{\varepsilon}}_R = \hat{\boldsymbol{\varepsilon}}_{\bar{\boldsymbol{u}}} \text{ with } \hat{\boldsymbol{\varepsilon}}_{\bar{\boldsymbol{u}}} \text{ arbitrary}; \qquad \forall\, \boldsymbol{x}_R \tag{39}$$

$$\hat{\boldsymbol{\beta}} \text{ arbitrary} \qquad \text{and} \qquad \hat{\boldsymbol{\varepsilon}}_R \equiv \boldsymbol{0}; \qquad \forall\, \boldsymbol{x}_\mathcal{S} \tag{40}$$

Remark 3.5 *In the following scale bridging variational equations, the macro-scale virtual strain actions, $\hat{\boldsymbol{\varepsilon}}_R$ and $\hat{\boldsymbol{\beta}}$, are arbitrary point-valued quantities at $\boldsymbol{x}$, i.e. $\hat{\boldsymbol{\varepsilon}}_R \in \mathbb{R}^{nd\times nd}_{sym}$ and $\hat{\boldsymbol{\beta}} \in \mathbb{R}^{nd}$ respectively ($\mathbb{R}^{nd\times nd}_{sym}$ is the vector space of symmetric second-order tensors).*

linked to a point $\boldsymbol{x}_R$ is expressed as:

$$\hat{\boldsymbol{\varepsilon}}_\mu = \hat{\boldsymbol{\varepsilon}}_{\bar{\boldsymbol{u}}} + \hat{\boldsymbol{\varepsilon}}_{\mu R} + \sum_{i=1}^{n_c} \left[\lim_{\ell_\mu^i \to 0} \phi_\mu^i \, \frac{\hat{\boldsymbol{\beta}}_\mu^i \otimes^s \boldsymbol{n}_\mu^i}{\ell_\mu^i} \right], \quad \forall\, \boldsymbol{y} \in \Omega_\mu. \tag{41}$$

Then, for any point $\boldsymbol{x}_R$, the Principle of Multiscale Virtual Power ([3]), accounting for possible nucleation of cohesive cracks only at the micro-scale, reads:

$$\boldsymbol{\sigma} \cdot \hat{\boldsymbol{\varepsilon}}_{\bar{\boldsymbol{u}}} = \frac{1}{|\Omega_\mu|} \int_{\Omega_\mu} \boldsymbol{\sigma}_\mu \cdot \hat{\boldsymbol{\varepsilon}}_\mu \, d\Omega_\mu, \quad \forall\, \hat{\boldsymbol{\varepsilon}}_{\bar{\boldsymbol{u}}} \in \mathbb{R}^{nd \times nd}_{\text{sym}},\ \forall\, \hat{\boldsymbol{\varepsilon}}_\mu \text{ kinematically admissible}, \tag{42}$$

where $\boldsymbol{\sigma}_\mu$ represents the micro-scale stress state, for which a constitutive law is required.

Considering (41) and (77) from Appendix I-(a), equation (42) can be re-written as:

$$\boldsymbol{\sigma} \cdot \hat{\boldsymbol{\varepsilon}}_{\bar{\boldsymbol{u}}} = \frac{1}{|\Omega_\mu|} \left[\int_{\Omega_\mu} \boldsymbol{\sigma}_\mu \cdot (\hat{\boldsymbol{\varepsilon}}_{\bar{\boldsymbol{u}}} + \hat{\boldsymbol{\varepsilon}}_{\mu R}) \, d\Omega_\mu + \sum_{i=1}^{n_c} \int_{\mathcal{S}_\mu^i} \boldsymbol{T}_\mu^i \cdot \hat{\boldsymbol{\beta}}_\mu^i \, d\mathcal{S}_\mu \right]$$
$$\forall\, \hat{\boldsymbol{\varepsilon}}_{\bar{\boldsymbol{u}}} \in \mathbb{R}^{nd \times nd}_{\text{sym}},\ \forall\, (\hat{\bar{\boldsymbol{u}}}_\mu, \hat{\boldsymbol{\beta}}_\mu^1, \ldots, \hat{\boldsymbol{\beta}}_\mu^{n_c}) \in \mathscr{V}_\mu^R, \tag{43}$$

with $\boldsymbol{T}_\mu^i$ denoting the cohesive traction acting on the micro-crack $\mathcal{S}_\mu^i$, for which a constitutive law is required.

3.3.2 Cohesive material regime at macro-scale

In this case, from (29) and taking definition (40) into consideration, the virtual kinematically admissible micro-scale strain field, $\hat{\boldsymbol{\varepsilon}}_\mu$, for an RVE linked to a point $\boldsymbol{x}_\mathcal{S}$ is expressed as:

$$\hat{\boldsymbol{\varepsilon}}_\mu = \sum_{j=1}^{n_{op}} \left[\lim_{\ell_\mu^{Lj} \to 0} \phi_\mu^{Lj} \, \frac{\theta\, \hat{\boldsymbol{\beta}} \otimes^s \boldsymbol{n}_\mu^{Lj}}{\ell_\mu^{Lj}} \right] + \hat{\boldsymbol{\varepsilon}}_{\mu R} + \sum_{i=1}^{n_c} \left[\lim_{\ell_\mu^i \to 0} \phi_\mu^i \, \frac{\hat{\boldsymbol{\beta}}_\mu^i \otimes^s \boldsymbol{n}_\mu^i}{\ell_\mu^i} \right], \quad \forall\, \boldsymbol{y} \in \Omega_\mu. \tag{44}$$

Then, for any point $\boldsymbol{x}_\mathcal{S}$, the Principle of Multiscale Virtual Power ([3]), accounting for cohesive cracks at both scales, reads:

$$\boldsymbol{T} \cdot \hat{\boldsymbol{\beta}} = \frac{1}{|\mathcal{S}_\mu^L|} \int_{\Omega_\mu} \boldsymbol{\sigma}_\mu \cdot \hat{\boldsymbol{\varepsilon}}_\mu \, d\Omega_\mu \quad ; \quad \forall\, \hat{\boldsymbol{\beta}} \in \mathbb{R}^{nd},\ \forall\, \hat{\boldsymbol{\varepsilon}}_\mu \text{ kinematically admissible}. \tag{45}$$

Considering (44) and (77) from Appendix I-(a), equation (45) can be re-written as:

$$\boldsymbol{T} \cdot \hat{\boldsymbol{\beta}} = \frac{1}{|\mathcal{S}_\mu^L|} \left[\theta \sum_{j=1}^{n_{op}} \int_{\mathcal{S}_\mu^{Lj}} \boldsymbol{T}_\mu^{Lj} \cdot \hat{\boldsymbol{\beta}} \, d\mathcal{S}_\mu + \int_{\Omega_\mu} \boldsymbol{\sigma}_\mu \cdot \hat{\boldsymbol{\varepsilon}}_{\mu R} \, d\Omega_\mu + \sum_{i=1}^{n_c} \int_{\mathcal{S}_\mu^i} \boldsymbol{T}_\mu^i \cdot \hat{\boldsymbol{\beta}}_\mu^i \, d\mathcal{S}_\mu \right]$$
$$\forall\, \hat{\boldsymbol{\beta}} \in \mathbb{R}^{nd},\ \forall\, (\hat{\bar{\boldsymbol{u}}}_\mu, \hat{\boldsymbol{\beta}}_\mu^1, \ldots, \hat{\boldsymbol{\beta}}_\mu^{n_c}) \in \mathscr{V}_\mu^\mathcal{S}, \tag{46}$$

with $\boldsymbol{T}_\mu^{Lj}$ (analogously to $\boldsymbol{T}_\mu^i$) denoting the cohesive tractions acting on the opening micro-cracks $\mathcal{S}_\mu^{Lj}$. Traction vectors $\boldsymbol{T}_\mu^{Lj}$ are obtained from a pre-defined constitutive law.

Remark 3.6 *No more hypotheses are introduced to complete the scale-transition model. The variational statements* (43) *and* (46) *contain all the required information to derive the remaining equations of the theory, that is, the homogenization rules for the macro-scale generalized stresses (the stress tensor and the cohesive traction) and the equilibrium problem at the RVE.*

macro-scale stress tensor, at $\boldsymbol{x}_R$, is obtained (consequence C1 of the formulation):

$$\boldsymbol{\sigma} = \frac{1}{|\Omega_\mu|} \int_{\Omega_\mu} \boldsymbol{\sigma}_\mu \, d\Omega_\mu. \tag{47}$$

Remark 3.7 *For points located in the compact support of $\boldsymbol{\beta}$ ($\boldsymbol{x}_R \in \Omega^\varphi$), the homogenization formula* (47) *depends on the tortuosity index θ, see Fig. 4. Let us recall that θ is one of the variables defining the insertion operator* (25)*, used to build the strain field $\boldsymbol{\varepsilon}_\mu$ at the micro-scale (refer to equation* (28)*). Thus, the micro-scale stress field $\boldsymbol{\sigma}_\mu$, of an RVE linked to $\boldsymbol{x}_R \in \Omega^\varphi$, depends on the θ-factor through $\boldsymbol{\varepsilon}_\mu$. The dependence of θ on $\boldsymbol{\sigma}_\mu$ is transferred to the homogenized stress, $\boldsymbol{\sigma}$, when expression* (47) *is applied.*

3.5 Traction homogenization on the cohesive interface (C2)

From (46), taking $\hat{\tilde{\boldsymbol{u}}}_\mu \equiv \boldsymbol{0}$, $\hat{\boldsymbol{\beta}}_\mu \equiv \boldsymbol{0}$ and arbitrary $\hat{\boldsymbol{\beta}} \in \mathbb{R}^{nd}$, the cohesive traction homogenization formula, for $\boldsymbol{x}_\mathcal{S}$, is derived (consequence C2 of the formulation):

$$\boldsymbol{T} = \frac{\theta}{|\mathcal{S}_\mu^L|} \Big[\sum_{j=1}^{n_{op}} \int_{\mathcal{S}_\mu^{Lj}} \boldsymbol{T}_\mu^{Lj} \, d\mathcal{S}_\mu \Big] = \frac{1}{\alpha} \Big[\sum_{j=1}^{n_{op}} \int_{\mathcal{S}_\mu^{Lj}} \boldsymbol{T}_\mu^{Lj} \, d\mathcal{S}_\mu \Big]. \tag{48}$$

From the definition of θ given by (27), the average factor $\alpha = |\mathcal{S}_\mu^L| \, \theta^{-1}$, present on the rightmost part of (48) yields:

$$\alpha = \frac{|\mathcal{S}_\mu^L|}{\theta} = \Big| \sum_{j=1}^{n_{op}} \int_{\mathcal{S}_\mu^{Lj}} \boldsymbol{n}_\mu^{Lj} \, d\mathcal{S}_\mu \Big|, \tag{49}$$

which can be geometrically interpreted as sketched in Fig. 5.

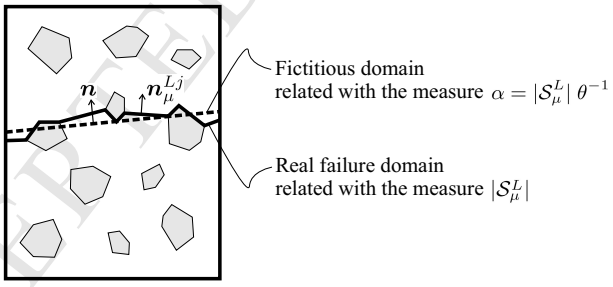

Figure 5: Geometrical interpretation for the parameter $\alpha = |\mathcal{S}_\mu^L| \, \theta^{-1}$, used as the averaging factor in the cohesive traction homogenization formula (48).

Remark 3.8 *The homogenized traction $\boldsymbol{T}$ depends explicitly on the tortuosity index θ through the leading term in* (48) *and implicitly through each micro-scale cohesive traction, $\boldsymbol{T}_\mu^{Lj}$, since the insertion operator $\boldsymbol{\mathcal{I}}_\mathcal{S}$ in equation* (26) *depends on θ. The implicit dependence can be explained following a similar constitutive-type argument as in Remark 3.7.*

Remark 3.9 *Although the tortuosity parameter has been introduced as a kinematical concept, through the definition of $\boldsymbol{\mathcal{I}}(\cdot)$, it has a fundamental effect on the homogenized responses for both macro-scale quantities $\boldsymbol{\sigma}$ and $\boldsymbol{T}$. The form in which the θ-factor influences the homogenization formulae* (47)-(48) *is not an a priori postulate of the model, but a natural consequence of the variational statement of the problem. Throughout the numerical simulations of Section 5, we show the importance of taking into account the tortuosity index properly, in order to obtain the correct mechanical response in the post-critical regime.*

(43), the equilibrium problem in the micro-scale domain involving possible nucleation of cohesive micro-cracks is derived (consequence C3 of the formulation). In a variational format it is stated as follows:

For any fixed time t and given the history of the regular macro-scale strains $\boldsymbol{\varepsilon}_R^t$, find $(d\tilde{\hat{\boldsymbol{u}}}_\mu, d\tilde{\hat{\boldsymbol{\beta}}}_\mu^1, \ldots, d\tilde{\hat{\boldsymbol{\beta}}}_\mu^{n_c}) \in \tilde{\mathscr{U}}_\mu^R$ such that:

$$\int_{\Omega_\mu} \boldsymbol{\sigma}_\mu \cdot \hat{\boldsymbol{\varepsilon}}_{\mu R}\, d\Omega_\mu + \sum_{i=1}^{n_c} \int_{\mathcal{S}_\mu^i} \boldsymbol{T}_\mu^i \cdot \hat{\boldsymbol{\beta}}_\mu^i\, d\mathcal{S}_\mu = 0, \quad \forall\, (\hat{\boldsymbol{u}}_\mu, \hat{\boldsymbol{\beta}}_\mu^1, \ldots, \hat{\boldsymbol{\beta}}_\mu^{n_c}) \in \mathscr{V}_\mu^R. \tag{50}$$

Consider now an RVE related to a point $\boldsymbol{x}_\mathcal{S}$ located at the cohesive macro-crack. Taking $\hat{\boldsymbol{\beta}} \equiv \boldsymbol{0}$ in expression (46), the micro-scale equilibrium problem in the presence of macro and micro-scale cohesive cracks is derived (consequence C3 of the formulation). In variational form it is stated as:

For any fixed time $t \in [t_N, \tau]$ and given the history of the regular macro-scale strains $\boldsymbol{\varepsilon}_R^t$ and the history of the macro-scale displacement discontinuity $\boldsymbol{\beta}^t$, find $(d\tilde{\hat{\boldsymbol{u}}}_\mu, d\tilde{\hat{\boldsymbol{\beta}}}_\mu^1, \ldots, d\tilde{\hat{\boldsymbol{\beta}}}_\mu^{n_c}) \in \tilde{\mathscr{U}}_\mu^\mathcal{S}$ such that:

$$\int_{\Omega_\mu} \boldsymbol{\sigma}_\mu \cdot \hat{\boldsymbol{\varepsilon}}_{\mu R}\, d\Omega_\mu + \sum_{i=1}^{n_c} \int_{\mathcal{S}_\mu^i} \boldsymbol{T}_\mu^i \cdot \hat{\boldsymbol{\beta}}_\mu^i\, d\mathcal{S}_\mu = 0, \quad \forall\, (\hat{\boldsymbol{u}}_\mu, \hat{\boldsymbol{\beta}}_\mu^1, \ldots, \hat{\boldsymbol{\beta}}_\mu^{n_c}) \in \mathscr{V}_\mu^\mathcal{S}. \tag{51}$$

3.7 Micro-scale constitutive model

In order to solve the variational problems (50) and (51), constitutive relations at the micro-scale must be prescribed for $\boldsymbol{\sigma}_\mu$ and $\boldsymbol{T}_\mu^i$ $(i = 1, \ldots, n_c)$, as functions of the histories of micro-scale regular strain and crack opening displacement. Symbolically, these response functionals (either phenomenological or obtained from an additional transition scale technique) can be expressed as follow:

$$\boldsymbol{\sigma}_\mu = \mathscr{F}_\mu(\boldsymbol{\varepsilon}_{\mu R}^t, \boldsymbol{\beta}_\mu^t), \quad \forall\, \boldsymbol{y} \in \Omega_\mu \backslash (\cup_{i=1}^{n_c} \mathcal{S}_\mu^i), \tag{52}$$

$$\boldsymbol{T}_\mu^i = \mathscr{T}_\mu^i(\boldsymbol{\varepsilon}_{\mu R}^t, \boldsymbol{\beta}_\mu^t), \quad \forall\, \boldsymbol{y} \in \mathcal{S}_\mu^i \quad i = 1, \ldots, n_c. \tag{53}$$

Typically, the stress tensor $\boldsymbol{\sigma}_\mu$ is characterized by means of a conventional constitutive model which include, for example, regularized softening-based evolution laws with damage, plasticity or any other dissipative mechanism.

On the other hand, the general setting adopted in the present paper to deal with strong discontinuity kinematics in the micro-scale (idealized as a limit case of strain localization bands), provides flexibility for choosing the family of constitutive models which characterize the cohesive traction evolution. This is an advantage of the proposed approach, in the sense that we can select one of the two well-known procedures, namely:

- The traditional cohesive model paradigm [4, 5], where the traction is univocally defined in terms of the (history of the) displacement jump on the crack faces.
- The Continuum Strong Discontinuity Approach to fracture [9–12], where the cohesive response in the interface discontinuity (i.e. the traction-separation law) is consistently derived from a regularized continuum stress-strain relation, valid on a strain localization band, whenever the thickness of such band approaches zero. This procedure allows to incorporate additional dependencies in the characterization of cohesive tractions in the RVE, as for example the triaxiality effect, a phenomenon recognized as fundamental in ductile failure analysis [64]. Obviously, this refined modeling capability is transferred to the homogenized traction constitutive law, at the macro-scale.

3.7.1 Specific constitutive model adopted at the micro-scale

Equations (52)-(53) represent general expressions to model the material behavior at the micro-scale. In the present work, degradation and failure mechanisms in the RVE-domain are accounted for by considering a regularized elastic-damage model, which is defined through the equations given in Box 1. Damage is allowed only under tensile stress states, a typical situation in quasi-brittle fracture simulations. The continuum damage

Cohesive tractions at the micro-scale, $\boldsymbol{T}^i_\mu$, are described by projecting the same continuum damage model onto the interface $\mathcal{S}^i_\mu$. In our formulation, this is achieved just by considering $\ell_\mu \to 0$, in the set of equations given in Box 1. More details about the formal derivation of cohesive models from regularized stress-strain continuum models can be found in [65].

4 Computational implementation

The numerical implementation of the multiscale model at both scales of analysis is based on the finite element method. Although the model assumes the existence of strong discontinuities at macro and micro-scales, and therefore the modeling of interfaces is required, different techniques are used in each case.

The macro-scale model uses a finite element technology with embedded strong discontinuities and automatic detection of the crack path. In Section 4.1, we present a brief summary of this approach.

An alternative methodology based on standard solid finite elements with high aspect ratios, mimicking micro-scale cohesive interfaces is briefly summarized in Section 4.2. A discussion about the adequate choice of the RVE boundary conditions and the numerical implementation is also addressed in that section.

The macro-scale numerical approach is able to handle strong discontinuities intersecting the mesh in arbitrary directions. However, considering that it requires significant computational efforts, we prefer a less demanding approach at the micro-scale, at the expense of giving up the ability to capture micro-cracks intersecting the finite element mesh in arbitrary directions.

4.1 Finite element technique at the macro-scale

A finite element with embedded strong discontinuities which has been conceived for the automatic identification of the geometrical positioning of the crack path, through a technique called "crack path field", is adopted to model the macro-scale. The numerical implementation of this method has been detailed elsewhere [66]. Hence, only the main issues related to this type of element are addressed here.

First, the concept of crack path field is briefly described, which is useful to detect the geometrical position of the discontinuity surface. Then, a finite element technique with embedded strong discontinuity, capable of modeling evolving cracks, is briefly summarized. Additional details of the complete procedure can be seen in the referenced work.

4.1.1 Crack path field technique

This procedure consists in evaluating the crack path-field $\kappa(\boldsymbol{x})$ and its zero level set Π:

$$\Pi = \{\boldsymbol{x} \mid \kappa(\boldsymbol{x}) = 0\} \tag{64}$$

Then, the set Π identifies the path of any evolving crack, see Fig 6, in the sense that:

$$\mathcal{S} \subset \Pi \tag{65}$$

The crack path field $\kappa(\boldsymbol{x})$ is the directional derivative (along a vector orthogonal to the crack path), of an internal variable, χ, projected onto a sufficiently smooth functional space. This variable χ must be subjected to a localization effect such that it should display an unbounded growth in $\mathcal{S}$, while remaining bounded and small in the regular part of the body. Typically, χ could be the equivalent strain in damage models.

The correct detection of Π is a key issue to embed a cohesive interface $\mathcal{S}$ satisfactorily into the finite element.

The generalization of the crack path field technique to the present multiscale modeling context demands an adequate definition of the field χ. It is defined by gathering information from the micro-scale, as follows:

$$\chi(\boldsymbol{x}) = \frac{1}{|\Omega_\mu|} \int_{\Omega_\mu} r_\mu \, d\Omega_\mu \tag{66}$$

where r_μ is the strain-like internal variable of the damage model describing the constitutive relation at the micro-scale level.

Box 1: Regularized tensile damage model at the micro-scale.

Elastic stress-strain relation

$$\boldsymbol{\sigma}_\mu = \frac{q_\mu}{r_\mu}\,\boldsymbol{C}^e_\mu\,\boldsymbol{\varepsilon}_\mu = [1-d_\mu(r_\mu)]\,\overbrace{\boldsymbol{C}^e_\mu\,\boldsymbol{\varepsilon}_\mu}^{\overline{\boldsymbol{\sigma}}_\mu} \tag{54}$$

$$d_\mu(r_\mu) = 1 - \frac{q_\mu(r_\mu)}{r_\mu} \tag{55}$$

Damage criterion

$$\mathscr{G}(\boldsymbol{\varepsilon}_\mu, r_\mu) = \sqrt{\overline{\boldsymbol{\sigma}}^+_\mu \cdot \boldsymbol{\varepsilon}_\mu} - r_\mu \leq 0 \tag{56}$$

$$\overline{\boldsymbol{\sigma}}^+_\mu = \sum_{i=1}^{3} \langle \overline{\sigma}_{\mu i} \rangle\, \boldsymbol{e}_i \otimes \boldsymbol{e}_i \tag{57}$$

Internal variable evolution laws with softening

$$\dot{r}_\mu = \gamma, \quad r_\mu|_{t=0} = r_{\mu 0} = \frac{\sigma_{\mu u}}{\sqrt{E_\mu}} \tag{58}$$

$$\dot{q}_\mu = \ell_\mu\, \overline{H}_\mu(r_\mu)\, \dot{r}_\mu, \quad q_\mu \geq 0, \quad q_\mu|_{t=0} = q_{\mu 0} = r_{\mu 0} \tag{59}$$

$$\overline{H}_\mu(r_\mu) = -\frac{r^2_{\mu 0}}{G_{f\mu}}\, \exp\left[-\frac{r_{\mu 0}}{G_{f\mu}}(r_\mu - r_{\mu 0})\right] \tag{60}$$

Loading/Unloading complementary conditions

$$\gamma \geq 0, \quad \mathscr{G} \leq 0, \quad \gamma\mathscr{G} = 0 \tag{61}$$

Tangent constitutive tensor

$$\text{if } \gamma = 0, \quad \boldsymbol{C}^{tan}_\mu = (1-d_\mu)\,\boldsymbol{C}^e_\mu \tag{62}$$

$$\text{if } \gamma > 0, \quad \boldsymbol{C}^{tan}_\mu = (1-d_\mu)\,\boldsymbol{C}^e_\mu - \left[\frac{q_\mu - \overline{H}_\mu\, r_\mu}{r^3_\mu}\right] \overline{\boldsymbol{\sigma}}_\mu \otimes \overline{\boldsymbol{\sigma}}^+_\mu \tag{63}$$

Material parameters that characterize the model

$\sigma_{\mu u}$: Ultimate tensile stress
E_μ : Young's modulus
ν_μ : Poisson ratio
$G_{f\mu}$: Fracture energy

Nomenclature definitions

r_μ : strain-like internal variable
q_μ : stress-like internal variable
d_μ : scalar damage variable
$\boldsymbol{C}^e_\mu$: isotropic elastic constitutive tensor
$\overline{\boldsymbol{\sigma}}_\mu$: effective stress state
$\overline{\boldsymbol{\sigma}}^+_\mu$: positive counterpart of effective stress state
$\overline{\sigma}_{\mu i}$: effective principal stress "i"
$\boldsymbol{e}_i$: eingenvector related to $\overline{\sigma}_{\mu i}$
$\langle\cdot\rangle$: Macaulay brackets
γ : damage consistency parameter
ℓ_μ : regularization parameter (thickness of strain localization band)
$\overline{H}_\mu$: intrinsic softening modulus (exponential degradation)

is implemented. This method has been used for single-scale failure analysis. Its generalization to the multiscale analysis is almost direct.

During the loading process, each quadrilateral finite element can switch between three different formulations, or states, denoted 0, 1 and 2, in accordance with the following criterion:

(i) Initially, elements in state 0 are modeled as standard quadrilaterals with bi-linear regular displacements.

(ii) Once the bifurcation condition is detected ($t = t_N$) in the central point of the element, it switches from state 0 to state 1. Elements in state 1 are also quadrilaterals with mixed interpolation: bi-linear interpolation for the incremental regular displacements and constant interpolation for the incremental regular strains. So, a quadrature rule with only one integration point is enough to evaluate consistently the integrals arising in the mixed formulation.

(iii) After a small loading increment, at the pseudo-time t_{SD} (with $t_{SD} > t_N$), elements in state 1 switch to state 2 and a strong discontinuity mode is embedded into the mixed quadrilateral finite element.

Fig. 6 provides additional details about the integration rule used in different states of the finite element during the loading process.

Before switching from states 1 to 2, the position of the interface $\mathcal{S}(\boldsymbol{x})$ must be determined according to the procedure given in Section 4.1.1. Placing the discontinuity surface $\mathcal{S}$ in the correct position avoids stress locking in elements where strain localization is taking place.

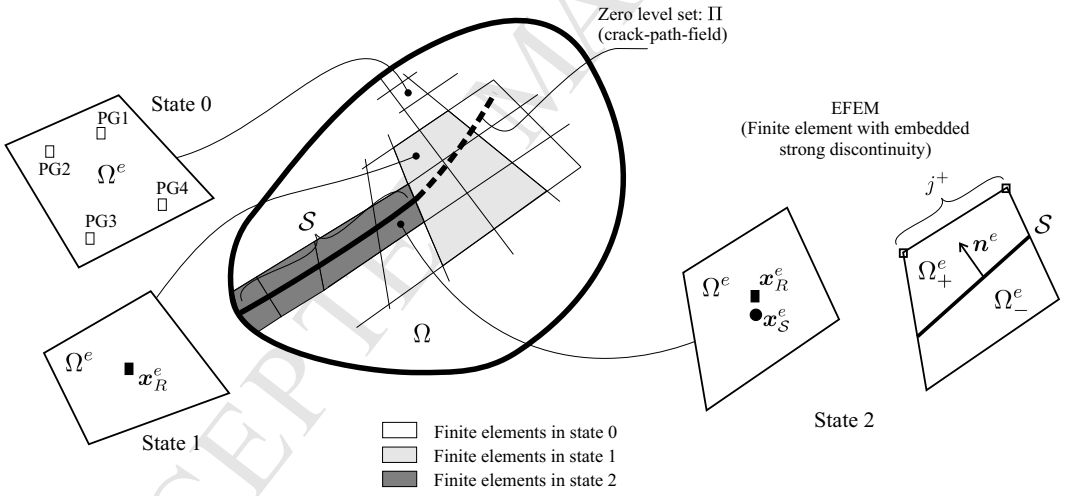

Figure 6: Finite element technique at the macro-scale. Quadrature points according to the element state: (i) elements in state 0 use the standard integration rule based on four Gauss points, (ii) elements in state 1 use only one quadrature point ($\boldsymbol{x}_R^e$) at the element center, (iii) elements with embedded strong discontinuities use two quadrature points ($\boldsymbol{x}_R^e$ and $\boldsymbol{x}_S^e$), both at the element center.

The finite element formulations for states 0 and 1 have been implemented following very standard procedures. The numerical implementation of finite elements in state 2, with embedded strong discontinuities and in the context of the present multiscale model, is briefly discussed here. More details on implementation will be addressed in a forthcoming contribution [67].

Note that only elements in state 2 are intersected by cracks. In this case, by construction, the support of $\boldsymbol{\varepsilon_\beta}$, see equation (9), is the element domain Ω^e. It means that elements having states 0 or 1 are outside the influence zone of any crack and the term $d\boldsymbol{\varepsilon}_\beta$ in equation (25) is $d\boldsymbol{\varepsilon}_\beta = \mathbf{0}$. Therefore, the insertion operator $\boldsymbol{\mathcal{I}}_R(d\boldsymbol{\varepsilon}_{\bar{\boldsymbol{u}}}, \mathbf{0})$, in elements with states 0 or 1, distributes uniformly the macro-scale strain $d\boldsymbol{\varepsilon}_{\bar{\boldsymbol{u}}}$ into the RVE. So, the multiscale model results identical to the conventional homogenization technique reported in the literature (see for example [36]), in the sense that the increment of macro-scale strain $d\boldsymbol{\varepsilon}_{\bar{\boldsymbol{u}}}$ is uniformly distributed in the RVE and the overall stress results in the standard volumetric average of the micro-scale stress field.

two-dimensional solid finite elements displaying very high aspect ratios. A similar technique has been reported in [68], where it has been shown that elements with increasing aspect ratios tend to capture a strong discontinuity kinematics [69]. Thus, this technique can be seen as an alternative procedure for modeling strong discontinuities arising across cohesive surfaces.

Degenerate Constant Strain Triangles (CST) are inserted between all the element edges of a predefined finite element mesh, as shown in Fig. 7. The geometrical distribution of degenerate CST elements is shown in gray, and their aspect ratio increases with $\ell_\mu^i \to 0$.

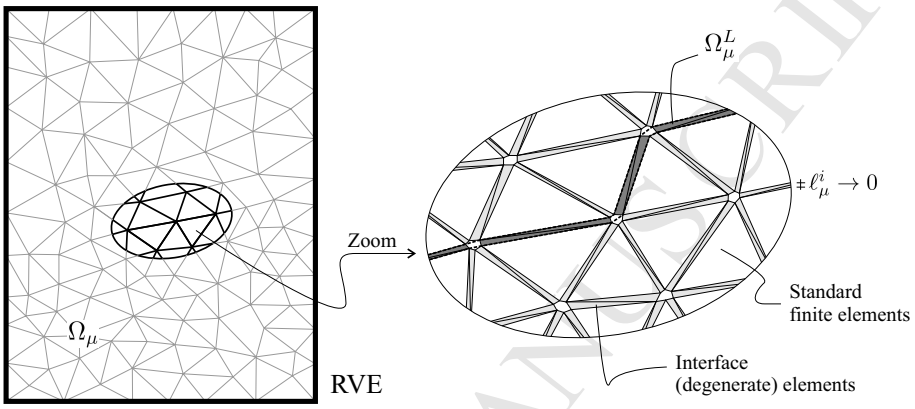

Figure 7: RVE finite element model with degenerate elements at all edges of standard finite elements. The thickness of the degenerate elements, ℓ_μ, tends to zero.

These degenerate elements are endowed with a continuum damage, or plastic-like, constitutive relation with strain softening (in the present contribution, the model presented in Box 1 has been adopted). The remaining finite elements could be endowed with an elastic or inelastic constitutive relation with hardening (in the present contribution, an isotropic elastic model has been adopted). Thus, evolving strain localization zones are restricted to domains determined by the degenerate elements with pre-defined thickness of size $\ell_\mu^i \to 0$.

In Fig. 8, we sketch the insertion of kinematical information from macro-to-micro scales. Note that according with the insertion operator $\boldsymbol{\mathcal{I}}_{\mathcal{S}}(d\boldsymbol{\varepsilon}_{\bar{u}}, d\boldsymbol{\varepsilon}_{\beta}, d\boldsymbol{\beta})$, see equation (26), the inserted macro-scale strain:

$$d\boldsymbol{\varepsilon}_{\bar{\boldsymbol{u}}} + \theta\, d\boldsymbol{\varepsilon}_{\boldsymbol{\beta}} + \left[\frac{\theta\, d\boldsymbol{\beta} \otimes^s \boldsymbol{n}_\mu^{L_j}}{\ell_\mu^{L_j}}\right], \tag{67}$$

is distributed in all the j-th degenerate elements which belong to Ω_μ^L (zone showed in dark gray in Fig. 8). The inserted macro-scale strain

$$d\boldsymbol{\varepsilon}_{\bar{\boldsymbol{u}}} + \theta d\boldsymbol{\varepsilon}_{\boldsymbol{\beta}} \tag{68}$$

is distributed in the remaining finite elements of the RVE, including the closing micro-cracks represented by the degenerated CST elements displayed in light gray in Fig. 8.

5 Numerical assessment of the multiscale model

5.1 Sensitivity analysis of the effective fracture energy with the tortuosity index

We assess the multiscale model for capturing the homogenized post-critical response. Specially, we evaluate the sensitivity of the effective fracture energy (G_f) and the total dissipated energy ($\mathscr{D}$) at the macro-scale, in terms of the crack path tortuosity at the RVE. This particular feature of the formulation is remarkably important to understand the role played by the material micro-structure in failure problems. The numerical tests presented in this section, although simple, have been conceived to demonstrate this.

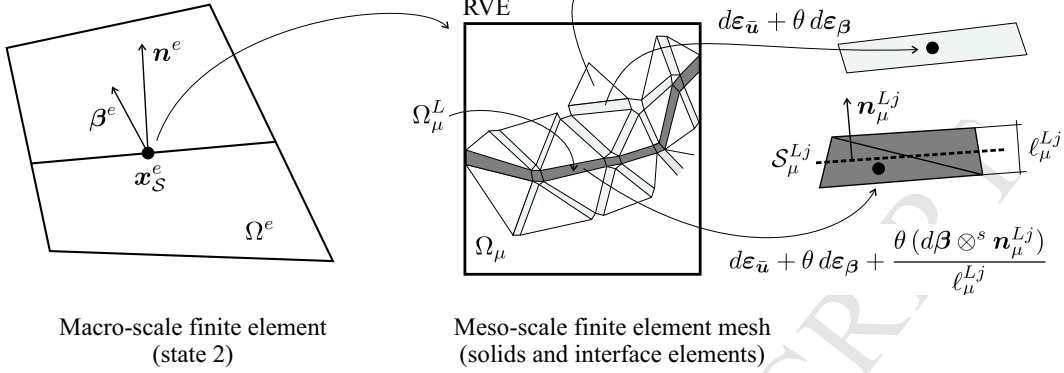

Figure 8: Insertion procedure of the kinematics related to a macro-scale integration point, $\boldsymbol{x}^e_{\mathcal{S}}$, into the RVE modeled with degenerate finite elements between interfaces.

5.1.1 Problem description

A homogeneous strip is considered as the macro-scale domain, see Fig. 9. The strip is subjected to a monotonically increasing vertical macro-scale displacement δ on the top edge, until the complete structural degradation is reached. The problem is analyzed assuming plane strain conditions.

Four periodic micro-structures of simple geometries are used as RVEs, see Fig. 9. At the micro-structures, pre-defined domains where cohesive cracks can be nucleated, are embedded into an elastic material matrix. Once the micro-scale cohesive cracks are nucleated, they are governed by a cohesive relation which is induced by a regularized continuum scalar damage model acting on a band of thickness ℓ_μ approaching 0 (see Section 3.7.1). The damage model degrades exponentially only under tensile states, therefore this behavior is inherited for the discrete-type cohesive law. The properties for the elastic matrix are: $E_\mu = 3.0e4$ [MPa] (Young modulus) and $\nu_\mu = 0.18$ (Poisson's ratio). The properties for the damage model are: $\sigma_{\mu u} = 2.6$ [MPa] (ultimate tensile stress), $G_{f\mu} = 2.0e2$ [N/m] (fracture energy), $E_\mu = 1.5e4$ [MPa] and $\nu_\mu = 0.18$. The material characterization is identical in the four RVEs considered.

The macro-scale homogenized responses are evaluated and compared according with two categories of micro-structures:

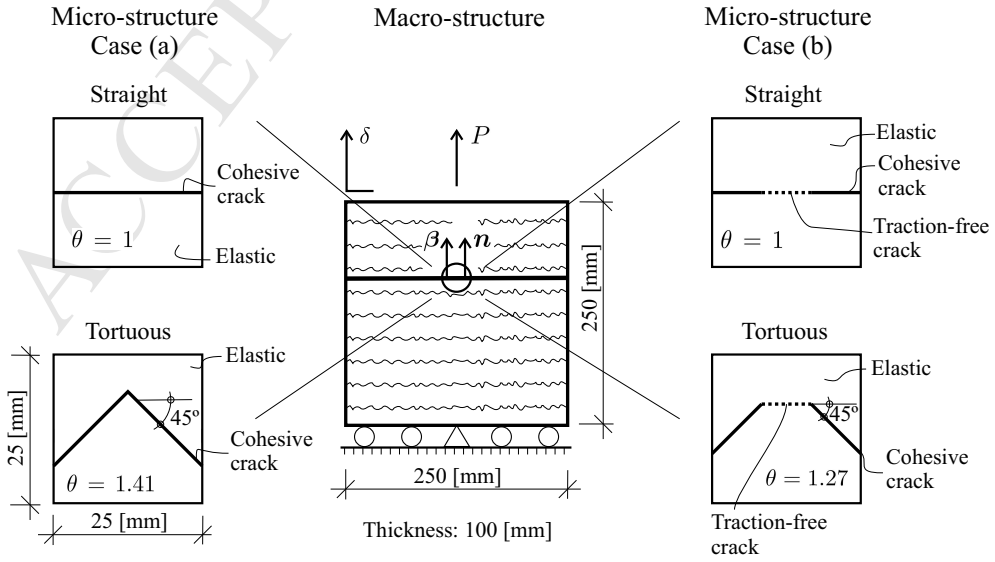

Figure 9: Strip subjected to uniaxial loading. Macro-scale mechanical model along with their corresponding micro-structural description.

$\theta = 1.41$, respectively.

Case (b): similar to the previous case, two micro-structures are compared (see Fig. 9-(right)). One with two horizontal cohesive cracks (solid lines) intersecting a horizontal traction-free crack (dotted line). The other with two slanted cohesive cracks at $\pm 45°$ (solid lines) intersecting a horizontal traction-free crack (dotted line). The total length of the slanted crack path is 27% longer than the length of the horizontal cracks. The corresponding tortuosity indices are $\theta = 1$ and $\theta = 1.27$, respectively.

After detecting bifurcation at macro-scale ($t = t_N$), the multiscale model considers that the overall fracture energy, in all cases, is represented by the nucleation of a unique and geometrically identical macro-crack, being orthogonal to the principal stretch direction (see Fig. 9-(center)). However, as we show next, stable material dissipation can take place at the macro-scale before the nucleation of the macro-crack, for $t < t_N$.

5.1.2 Multiscale model vs. Direct Numerical Simulation

The total expended external energy, required to exhaust the structural load carrying capacity, is studied using the proposed multiscale (MS) model. Results are compared with DNS (Direct Numerical Simulation) solutions that are assumed as the reference accurate responses.

The MS finite element models are shown in Fig. 10. At the macro-scale, only one finite element with embedded strong discontinuity (see Section 4.1.2) is used. Thus, the fracture process of the strip is highly idealized. Even so, we show that MS formulation provides solutions which compare very well with the refined DNS method. The RVE finite element meshes are also observed in Fig. 10, for each analyzed case. Periodic boundary conditions are assumed for the external RVE boundary (SBC): points on the solid lines are paired with points on the dotted lines. The vertex nodes are fixed (zero displacement fluctuations). This set of kinematical restrictions is a particular case of the minimally constrained vector space $\tilde{\mathscr{U}}_\mu^R$ (and $\mathscr{V}_\mu^R$). Once the macro-crack is nucleated, (incremental) displacement fluctuations at the RVE-domain are fixed to zero, a particular case of $\tilde{\mathscr{U}}_\mu^{\mathcal{S}}$ (and $\mathscr{V}_\mu^{\mathcal{S}}$).

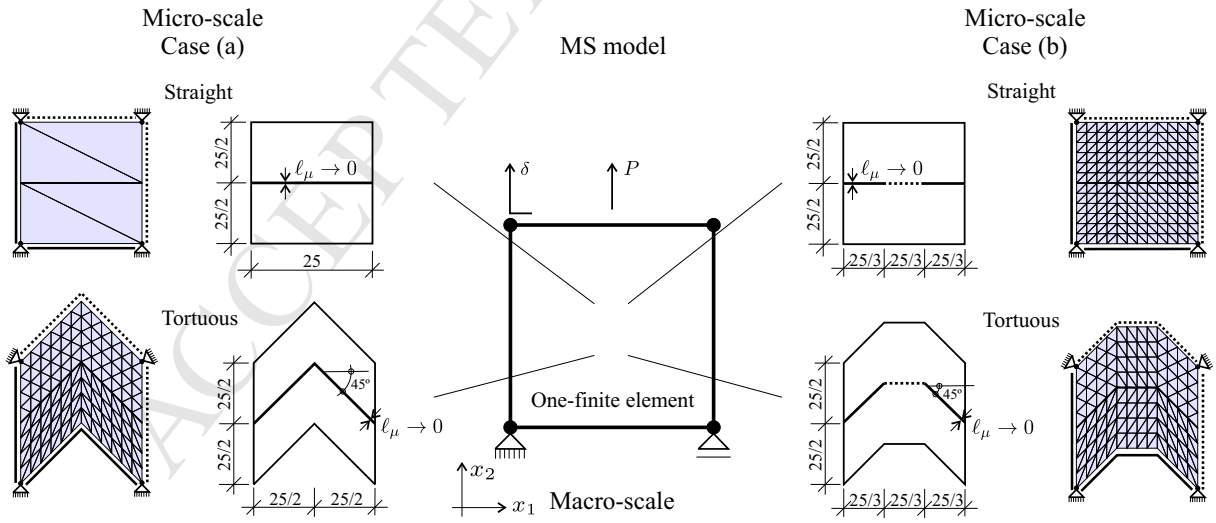

Figure 10: Strip subjected to uniaxial loading. Discrete models for the MultiScale (MS) formulation: macro-scale model (one finite element) and RVE finite element models for the four micro-structures (periodic boundary conditions are considered between solids and dotted external boundaries). Units of length in millimeters.

The DNS finite element meshes are built by horizontal and vertical repetition of the discrete periodic cells shown in Fig. 11 where only the tortuous cases are displayed. Identical material properties and distributions as in the RVEs of the multiscale model are assumed.

Fig. 11 (center) depicts a comparative analysis of the damage levels observed in both, MS and DNS solutions, at the bifurcation time ($t = t_N$). Even though the DNS solutions show a slight non-uniform damage distribution

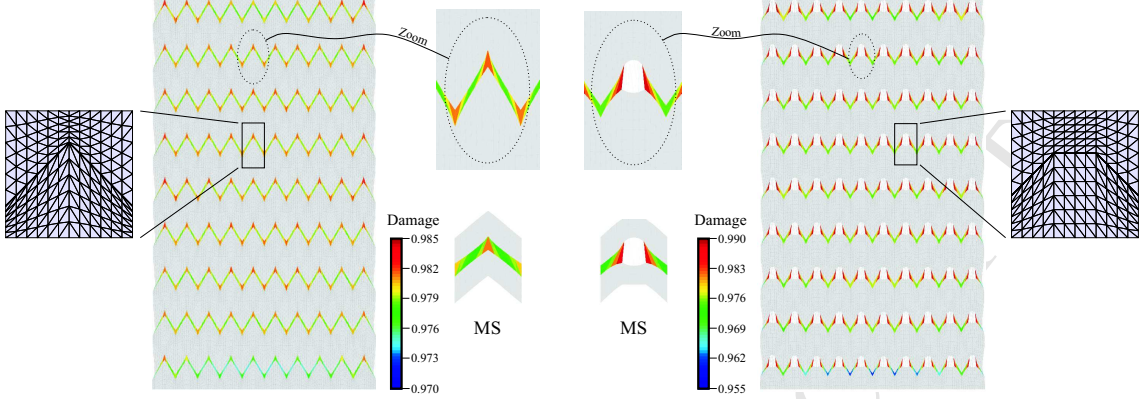

Figure 11: Strip under uniaxial loading. DNS finite elements models for the tortuous path cases. Comparative analysis of the damage solutions given by DNS and MS models, at the macro-scale bifurcation time ($t = t_N$).

in bands at different heights and the MS model is macroscopically homogeneous (prior to bifurcation), the solutions obtained with both models compare very well in terms of qualitative results. The slight non-uniformity observed in the DNS responses is due to initial perturbations imposed to trigger the strain localization in the central zone of the strip.

The external total force (P) vs. vertical displacement (δ) curves are exhibited in Fig. 12, using both techniques MS and DNS. Note that MS model provides very accurate results, if compared with the DNS solutions, in terms of initial overall elasticity, non-linear stable dissipation, peak load detection and the complete post-critical equilibrium branch. Therefore, the total dissipated energy, $\mathscr{D}$, predicted by the MS and DNS models (the areas under the P-δ curves), are in very close agreement in both cases (tortuous and straight cracks).

5.1.3 Discussion of results

First, let us focus on Case (a). The crack path tortuosity introduces two noteworthy effects: (i) an increase of the peak load P_u, from about $P_u = 6.8e4$ [N] (for $\theta = 1$) to $P_u = 7.8e4$ [N] (for $\theta = 1.41$), as seen in Fig. 12-(a) and (ii) the existence of a stable (distributed) energy dissipation regime prior to macro-scale bifurcation ($t < t_N$) in the tortuous case, see the non-linear P-δ response before reaching the limit load in insert of Fig. 12-(a). These results can be explained as follows. Although the stretching process is uniform at the macro-scale, crack path tortuosity induces a non-uniform stress state at the micro-scale. Therefore damage evolves describing non-uniform patterns (see Fig. 11). Low values of damage in the RVE are not enough to induce softening and material bifurcation at the macro-scale. In fact, as shown Fig. 11, levels of damage greater than 0.97 are required to achieve macro-scale bifurcation and, as a consequence, the nucleation of the macro-crack. The evolution of this inelastic process at the micro-scale (from the onset of damage to damage near 0.97) is transferred to the macro-scale as an irreversible mechanism of stable dissipation, which takes place along the whole volume of the strip, increasing the effective ductility of the material. Observe that one part of what is defined as *fracture energy* (per unit area) in the RVE, $G_{f\mu}$, characterizing the micro-scale cohesive laws, develops during the (volumetric) *stable energy dissipation* at the macro-scale. Then, the micro-scale energy released during the stable dissipation regime at macro-scale level is not available to contribute to the effective macro-scale fracture energy G_f, i.e. the fracture energy (per unit area) required to degrade the macro-scale cohesive crack. From the comparison with the reference DNS solution, we conclude that the proposed multiscale model is able to deal with this complex phenomenology involving non-trivial relationships between energy measures with dissimilar dimensionality. As the stable dissipation process develops in the tortuous Case-(a), the total external load increases until it reaches a peak, P_u, which is greater than the peak load obtained without crack tortuosity.

The overall fracture energy, G_f, is obtained through integration of the macro-scale traction vs. crack opening response $\boldsymbol{T}$-$\boldsymbol{\beta}$. Considering Case-(a), we have: $G_f = 0.20$ [N/mm] (for $\theta = 1$) and $G_f = 0.196$ [N/mm] (for $\theta = 1.41$), the last value represents the area below the blue curve T_{x_2} vs β_{x_2} in Fig. 13-(b). In this example, the effective fracture energy available to exhaust the macro-scale cohesive crack, linked to a tortuous path in the RVE ($\theta = 1.41$), is smaller than the value corresponding to the macro-crack related to aligned micro-cracks

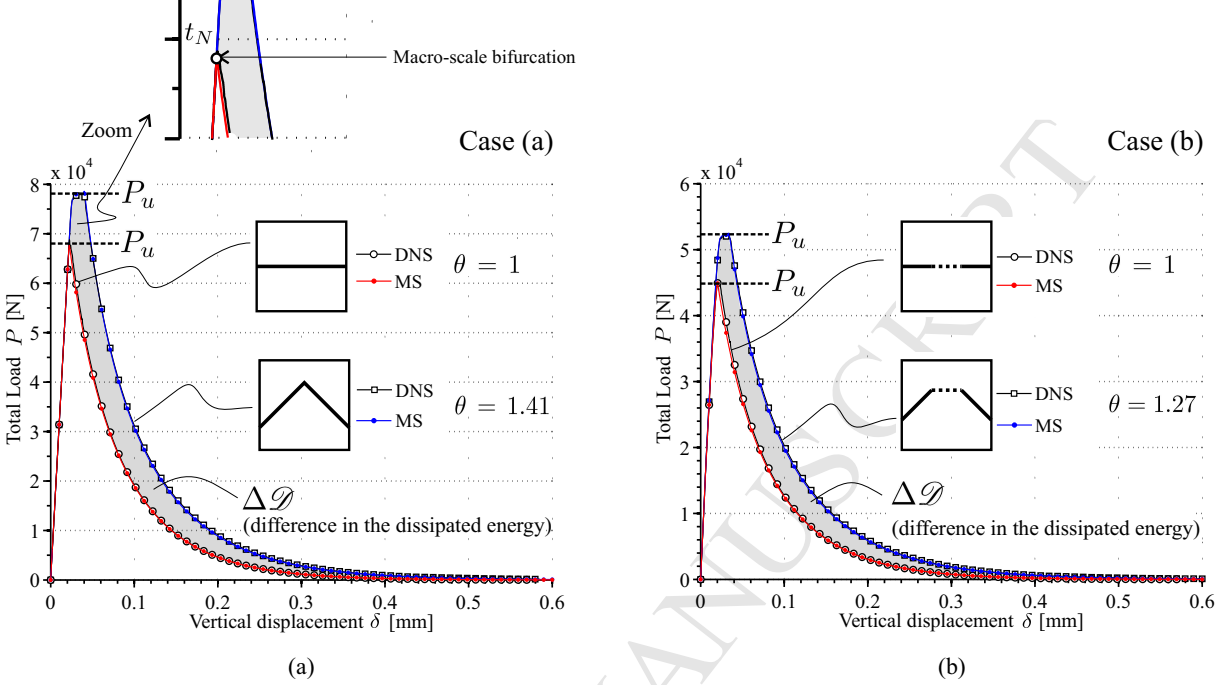

Figure 12: Strip under uniaxial loading. P vs. δ curves at the macro-scale, obtained using MS and DNS approaches.

($\theta = 1$). However, the total expended external work to get complet degradation ($\mathscr{D}$) for the micro-structure with zig-zag cohesive cracks is 51% larger than that computed with the micro-structure having an horizontal cohesive crack (see gray zone in Fig. 12-(a)). These results confirm that, even simulating horizontal macro-cracks opening in Mode I, the structural response obtained with the MS model distinguishes between distinct crack path tortuosities at the micro-scale, , in both cases.

Similar conclusions are obtained analyzing the plots in Fig. 12-(b) corresponding to Case-(b), where pre-existing traction-free micro-cracks have been considered. Thus, we can conclude that the tortuosity index θ, included in the MS formulation, has the correct mechanical effect on the homogenized responses.

In order to highlight the previous conclusion, additional results are shown in Fig. 13 and Fig. 14. We compare the homogenized responses using slight variations of the proposed MS model (denoted MS_A and MS_B models), applied to Case (a)-tortuous ($\theta = 1.41$):

- The MS_A-model solution fully removes the tortuosity parameter by setting $\theta = 1$ in all the scale bridging equations.

- The MS_B-model solution corresponds to a multiscale methodology where the tortuosity index is only considered in the definition of the $\boldsymbol{\mathcal{I}}_{\mathcal{S}}(\cdot)$-operator, but it is not accounted for in the regular insertion counterpart $\boldsymbol{\mathcal{I}}_{R}(\cdot)$ (see (26) and (25), respectively). This method (MS_B) neglects the influence of tortuosity factor on the evaluation of the macro-scale stress tensor in regular points $\boldsymbol{x}_R \in \Omega \backslash \mathcal{S}$, near the macro-crack.

Let us consider the macro-scale point $\boldsymbol{x}$ where at time $t = t_N$ a cohesive interface with the normal vector $\boldsymbol{n} = [n_{x_1}\ n_{x_2}] = [0\ 1]$ is introduced (see Fig. 13). We analyze the continuity of the normal component of the traction vector provided by the MS model, before and after the interface insertion ($\sigma_{x_2x_2} = \boldsymbol{\sigma} \cdot (\boldsymbol{n} \otimes \boldsymbol{n})$ for $t \leq t_N$ and T_{x_2} for $t > t_N$). Fig. 13-(a) depicts the homogenized constitutive response ($\sigma_{x_2x_2}$ vs. $\varepsilon_{x_2x_2}$) before detecting macroscopic bifurcation ($t < t_N$) while Fig. 13-(b) shows the homogenized cohesive response (T_{x_2} vs. β_{x_2}) once the macro-crack is nucleated ($t > t_N$). Even in this simple numerical experiment, and according to the different scale bridging equations (given by MS, MS_A or MS_B models), a very sensitive response with respect to θ can be observed. The MS_A-model shows a marked discontinuous behavior at t_N, i.e. when the peak load P_u is reached (see Fig. 13-(b)). Thus, using the MS_A technique, the transition from a classical homogenization

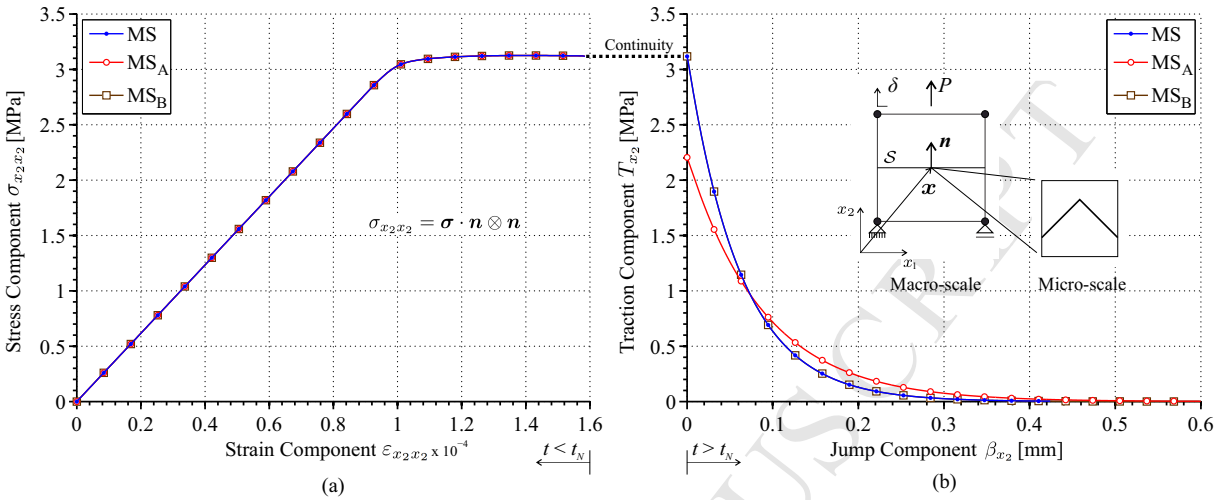

Figure 13: Strip under uniaxial loading (Case (a)-tortuous): (a) $\sigma_{x_2\,x_2}$ vs. $\varepsilon_{x_2\,x_2}$ homogenized response before detecting macro-scale bifurcation, (b) T_{x_2} vs. β_{x_2} homogenized response after nucleation of macro-scale cohesive crack. Solutions obtained using MS, $\mathrm{MS_A}$ and $\mathrm{MS_B}$ approaches.

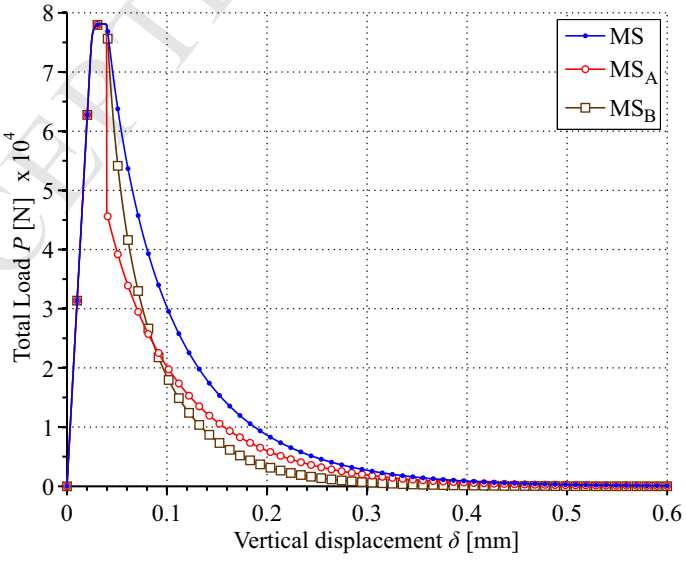

Figure 14: Strip under uniaxial loading (Case (a)-tortuous). P vs. δ curves at the macro-scale level. Solutions obtained using MS, $\mathrm{MS_A}$ and $\mathrm{MS_B}$ approaches.

when it is inserted into the RVE-domain. A similar inconsistent response is also observed in the structural load-displacement P-δ curve of Fig. 14. The MS_B-model, which only accounts for a scaling of $d\boldsymbol{\beta}$ (through θ) during the kinematical transfer related to $\boldsymbol{x}_\mathcal{S}$, eliminates the discontinuous response and furthermore provides identical T_{x_2}-β_{x_2} response as the MS-model (see Fig. 13-(b)). However the MS_B-solution is still mechanically inconsistent, since it does not provide the correct post-critical structural behavior (see Fig. 14), showing an effective energy dissipation which is different from the DNS solutions (here DNS and MS give almost identical responses). Thus, the importance of considering the tortuosity parameter in the insertion procedure for regular points, located in the compact support of $\boldsymbol{\beta}$ ($\boldsymbol{x}_R \in \Omega^\varphi$), is clear.

5.2 Multiscale analysis of a concrete-like material

5.2.1 Modeling of concrete failure

A concrete-like material is considered by modeling its meso-structure[7]. Concrete is a typical example of a non-periodic and quasi-brittle heterogeneous material. At the meso-scale, two main phases can be recognized: the cementitious matrix and the coarse aggregates. Failure generally initiates at the interface between matrix and aggregates, and cracks propagate across the matrix. In general, for low-to-moderate strength concretes, trans-aggregate fracture is never observed[8]. Then, from the material failure viewpoint, (low-to-moderate strength) concrete can be modeled at meso-scale by incorporating three constituents: (i) the matrix-aggregate interface, which is the weakest phase of the composite, (ii) the cementitious matrix which also can be subjected to cracking and degradation and (iii) the aggregates which behave elastically with no degradation at all. Based on these modeling assumptions, we develop a meso-scale model for concrete failure following very closely the approximations reported in Carol et al. [70] and Unger et al. [71].

Meso-structure generation

The representation of a plane strain state in concrete, at the meso-scale level, is idealized by selecting different shapes/sizes of rigid particles, which correspond to a given type of coarse aggregate, and distributing them randomly into the micro-cell. The particle shapes are randomly selected from a pre-defined set of irregular polygons, typifying granitic-type coarse aggregate. The coordinates for each particle centroid are selected randomly following a uniform probability distribution; the orientation angle for each aggregate is also random. A exclusion zone around previously generated particles is considered. The total number of particles and their sizes (between 3 [mm] and 5 [mm]) are computed such that a pre-assumed coarse aggregate volume fraction, ω_{Agg}, is reached. Following to [71], we have adopted $\omega_{Agg} = \frac{\text{Aggregate volume}}{\text{Total RVE volume}} \times 100 = 20.7\%$. The RVE size is 25.0 [mm] $\times$ 25.0 [mm], and the average aggregate size is 3.43 [mm], see Fig. 15.

According to the finite element technique adopted to simulate the RVE, as explained in Section 4.2, the meso-scale finite element model is designed as shown in Fig. 15. Interface elements are inserted along the matrix-aggregate interfaces, as well as along the interfaces of the matrix finite elements.

All the interface elements are subjected to material degradation. The constitutive model representing the mechanical response of both interfaces, matrix-matrix and matrix-aggregate, is the regularized isotropic damage model with exponential softening discussed in Section 3.7.1. Since the thickness of interface elements is very small, the continuum damage model degenerates into a cohesive-type constitutive law which characterizes the mechanical behavior of the cracks at the micro-scale level. Damage in the cementitious matrix is only allowed through the embedded interface elements. Material parameters are presented in Table 1.

5.2.2 Strip subjected to uniaxial strains. Analysis of boundary condition effects on the RVE failure mode capturing

A macro-scale strip is subjected to uniaxial stretching in different directions, while the associated micro-cells are attached to a fixed reference frame $\{y_1, y_2\}$ (see Fig. 16). Therefore, the principal macro-scale stress direction for each test displays a different orientation with respect to the micro-scale fixed reference system. It is expected

[7] In the applications involving concrete-like materials, the term meso-structure or meso-scale identifies the smaller length scale of the multi-scale model. Thus, the prefix "meso" should be considered as a synonym for the prefix "micro", used in this work.

[8] Trans-aggregate fracturing can be observed in high strength concretes.

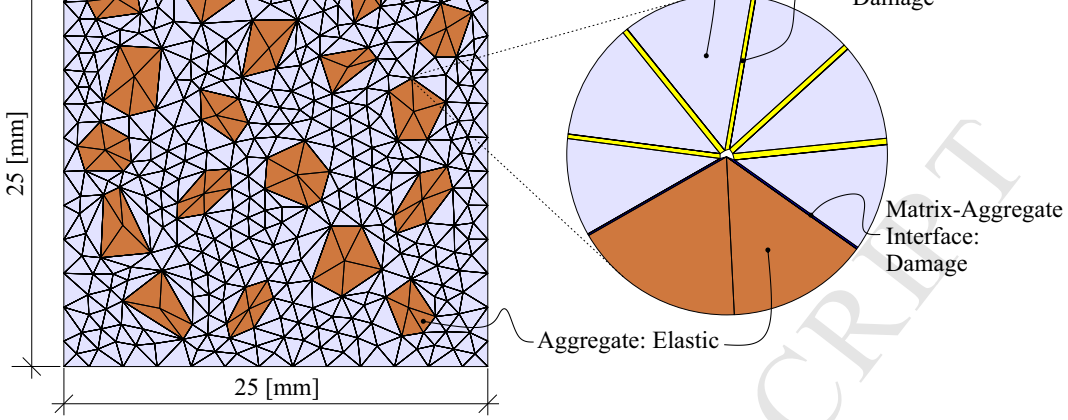

Figure 15: Concrete meso-scale model (average size of the matrix finite elements: 1.30 [mm]). Detail of the continuum and embedded interface finite elements.

	E_μ [MPa]	ν_μ	$\sigma_{\mu u}$ [MPa]	$G_{\mu f}$ [N/m]
Elastic cementitious matrix	1.85e4	0.18	—	—
Elastic aggregate	3.70e4	0.18	—	—
Matrix-matrix interface	1.85e4	0.18	2.60	140
Matrix-aggregate interface	1.85e4	0.18	1.30	70

Table 1: Material properties for the meso-structure depicted in Fig. 15, taken from [71].

that the failure path at the micro-scale level results (in an averaged sense) almost orthogonal to the homogenized tensile stress direction (loading direction).

The dimensions of the macro-structure are 125.0 [mm] × 125.0 [mm] and the thickness is 100 [mm], see Fig. 16. Plane strain condition is assumed.

The objective of this numerical test is twofold:

- First, we assess the capability of the micro-scale finite element model to capture failure modes at different directions relative to the RVE axis, depending on the macro-scale stretching orientation. In this context, the selection of appropriate kinematical constraints, on the RVE boundaries, is a fundamental issue to be considered. Very restrictive kinematical constraints can inhibit, or delay, the nucleation of micro-cracks near the RVE boundaries, as well as the macro-scale bifurcation time, giving rise to a spurious effective mechanical response.

- Second, we compare the homogenized load-displacement structural responses under changes in the macro-scale stretching direction. Thus, we study if the adopted micro-cell design (RVE size, aggregate location/distribution, etc.) retrieves an isotropic macro-scale response, during the pre-critical and post-critical regimes, in terms of a uniaxial loading process.

Summarizing, we assess the ability of the prescribed boundary conditions at the RVE in capturing the expected fracture pattern, the macroscopic bifurcation time, the homogenized peak load and the post-critical response, according to changes in the principal direction of the overall stress. The macroscopic responses have to be almost identical and independent of the stretching direction.

A schematic description of the tests is shown in Fig. 16-(top). The stretch direction forms an angle η with the horizontal line. For each η, the same meso-structure is represented by the corresponding RVE, also shown in the same figure. Boundary conditions on the RVE-boundaries (SBC) consider: (i) zero (incremental) fluctuation displacements for the four corner nodes of the RVE plus (ii) the minimum kinematical constraint, given by equation (34). Therefore, the adopted kinematical space for the SBC characterizes a multiscale sub-model which is between the minimally constrained and the classical periodic sub-models. The specification of

of the minimally constrained space $\tilde{\mathscr{W}}_{\mu}^{\mathcal{S}}$.

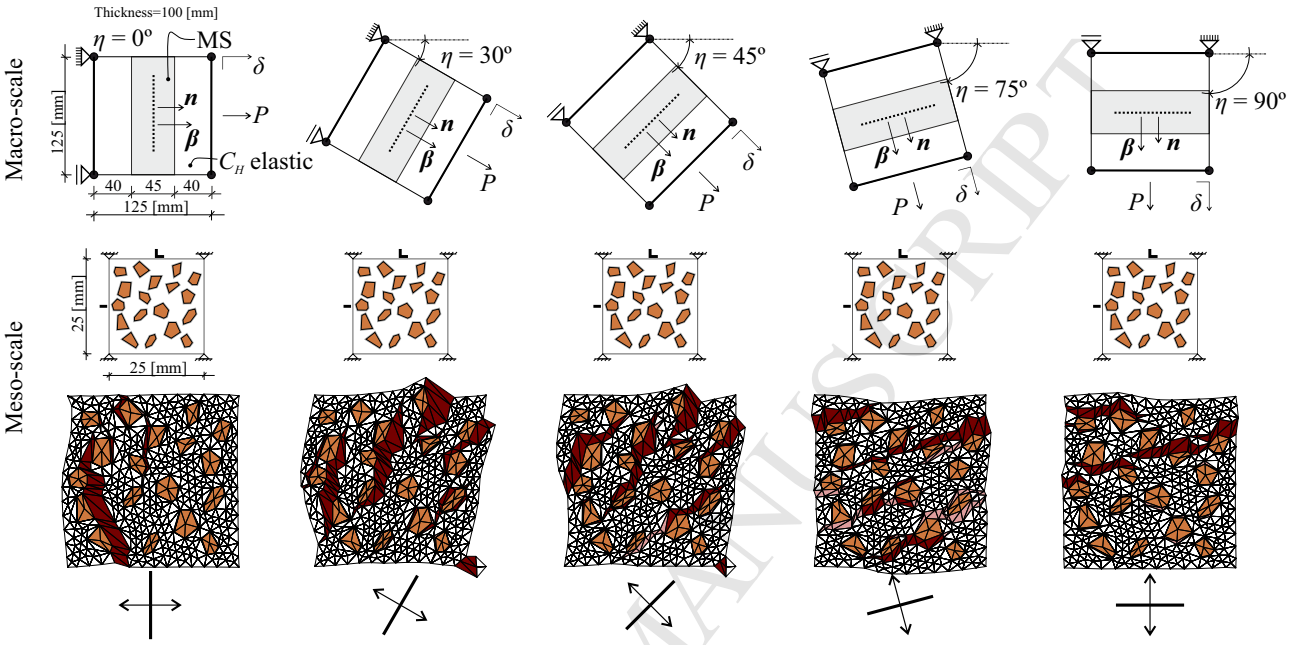

Figure 16: Macro-scale strips with concrete-like meso-structure. Configuration of the rotating macro-structure according with the angle η (top). Fixed RVE with their corresponding boundary conditions (middle); short black lines show the degree of freedoms where the minimum kinematical constraints are imposed. Deformed configuration of the RVE at the nucleation time t_N, for each macro-scale stretching orientation (bottom).

At the macro-scale, three quadrilateral finite elements are considered (see Fig. 16-(top)). Only the central macro-scale element can nucleate a cohesive crack, as explained in Section 4.1.2. The remaining two finite elements behave elastically, with a constitutive tensor $\boldsymbol{C}_H$ obtained after homogenization of the concrete-like meso-structure during a purely elastic loading process. The stretching orientations are defined by the angles $\eta = 0°$, $15°$, $30°$, $45°$, $60°$, $75°$ and $90°$ with the horizontal axis. The RVE-discrete model can be observed in Fig. 15.

Fig. 16-(bottom) also displays the deformed configurations at $t = t_N$ (according to the displacement fluctuation field) and the fracture patterns of the RVEs, for different cases. Opening cohesive micro-cracks are shown in deep red (those within the interface domain $\mathcal{S}_{\mu}^{L}$), while closing micro-scale cohesive cracks are shown in light red. For all cases, the RVE deformed configurations display a rather clear tendency to nucleate cracks which are orthogonal (in an averaged sense) to the macro-scale principal stress direction. Thus, we conclude that the obtained meso-scale failure modes are mechanically consistent with the macro-scale stretching orientation.

Fig. 17-(a) compares several curves of macro-structural responses (P vs. δ), parameterized with the angle η. We assume that solutions with $\eta = 0°$ and $\eta = 90°$ correspond to a similar test. Then, variability in the structural results for both cases is explained by the fact that these cases correspond to two instances of the same material, using different windows to represent the mesoscopic behavior.

Summarizing, the proposed multiscale model is able to capture complex failure modes at the RVE level (comprising multiple, tortuous and disconnected micro-cracks) whose homogenized mechanical response is almost insensitive to the macro-scale stretching direction.

Evaluation of the minimum mesoscopic cell size satisfying the condition to be an RVE, as well as the important question of the insensitivity of θ with finite element mesh size, will be presented elsewhere [67].

5.2.3 The L-Panel test

The objective of this test is to assess the ability of the multiscale failure model in simulating a more realistic concrete fracture process observed in the L-shaped panel of Fig. 18-(a). This specimen has been tested and

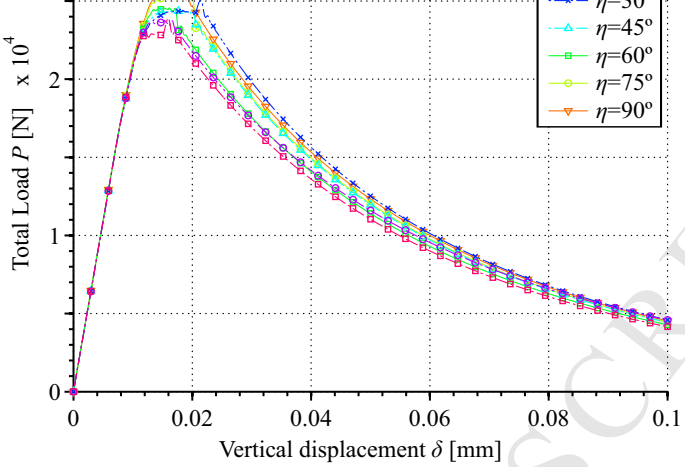

Figure 17: Macro-scale strip with a concrete-like meso-structure. Load vs. displacement curves for different stretching orientations.

reported in [72]. The test setting and the geometry of the specimen are shown in Fig. 18. The thickness of the L-panel is 100 [mm]. Plane strain state is assumed.

The meso-scale model is identical to that presented in Section 5.2.1. Material parameters and aggregate volume fraction agree with those reported in [71].

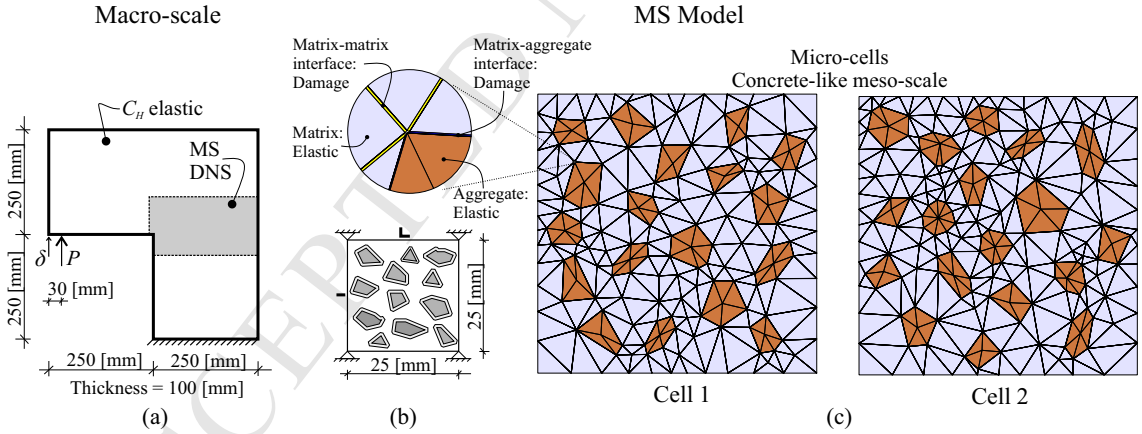

Figure 18: L-Panel test: (a) Setup and geometry of the macro-scale specimen, (b) Size and Standard Boundary Conditions (SBC) prescribed on the mesoscopic cells, (c) Finite element meshes for Cell 1 and Cell 2 (average size of the matrix finite elements: 2.10 [mm]).

Four solutions based on MS and DNS simulations have been obtained to compare the specimen fracture response and its sensitivity to the meso-structure design:

- Two MS simulations with different distribution of aggregates, are considered (see Fig. 18). In order to analyze the dispersion of results due to the meso-structure design, two micro-cells with random distribution and shape of aggregates are used in the simulations (Cell 1 and Cell 2). Their finite element models are shown in Fig. 18-(c).

  Fig. 18-(b) displays the micro-cell size and the Standard Boundary Conditions (SBC) that are prescribed for the pre-bifurcation regime ($t < t_N$). The SBC are minimum kinematical constraints with the four vertices fixed. The short black lines on the RVE-boundaries show the degree of freedoms where the minimum kinematical constraints are imposed, (see [2] for additional details). Once a macro-crack is

Only the domain shown in gray in Fig. 18-(a), at the macro-scale, is simulated with a MS model. The remaining part of the specimen is assumed to be linear elastic. In the elastic domain, the elasticity tensor $\boldsymbol{C}_H$ is the overall elastic one obtained by homogenization of the purely elastic response of the same mesoscopic cells and SBC adopted for the analysis.

- Two DNS simulations are considered, see Fig. 19-(a). In these cases, the concrete is modeled with similar details to those used at the meso-scale. Then, aggregates, matrix and interfaces are introduced in the analysis with identical parameters to the corresponding MS models.

  Two different meso-structure designs are adopted: Meso-structure 1 and Meso-structure 2, as shown in Fig. 19-(a). Again, the DNS analyzes with both meso-structures give information about the dispersion of numerical results obtained by different distribution of heterogeneities.

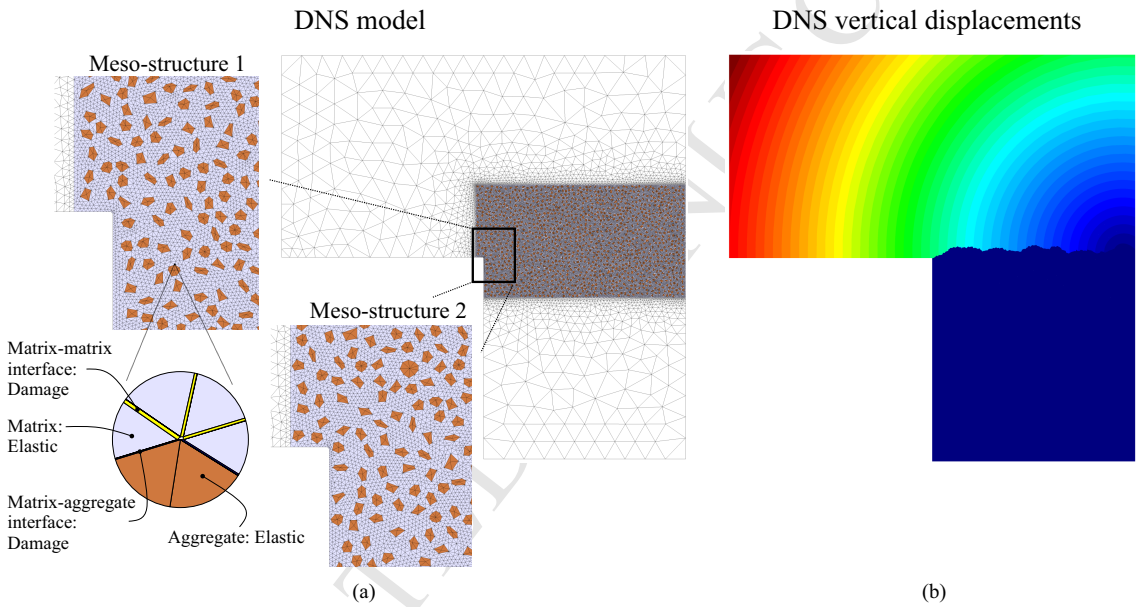

Figure 19: L-Panel test. DNS models: (a) Finite element mesh and details for Meso-structures 1 and 2 (average size of the matrix finite elements: 1.05 [mm]), (b) Contour fill map of vertical displacements.

Fig. 20-(a) plots the structural response in terms of the P vs. δ curves. The four numerical solutions show a slow dispersion and fit very well within the envelope of experimental results. Fig. 20-(b) compares the macro-scale crack paths obtained using the finite element models, DNS and MS simulations, with the experimental failure pattern (gray zone in Fig. 20-(b)). The macro-scale crack path for the DNS method (that related to Meso-structure 1) can be obtained from Fig. 19-(b), by post-processing the predicted localization zone of the vertical displacement field. In the case of MS models (Cell 1), the macro-scale crack path is a direct result of the formulation.

Fig. 21 displays the results obtained with the MS model and Cell 1. The finite elements at the macro-scale level with embedded cohesive cracks are colored in deep red. The blue line, intersecting those elements, is the predicted zero level set π of the crack path-field technique. The normal vectors to the macro-crack are also depicted. These vectors are the average of the normal vectors to the opening set of cohesive cracks in the mesoscopic cell. In the same figure, a number of deformed configurations, in terms of the RVE fluctuation displacement field, are shown. They correspond to different points along the propagating macro-scale cohesive crack, at each nucleation time t_N. Note that the failure modes at the meso-scale level are in good agreement (in an average sense) with the macro-crack orientation.

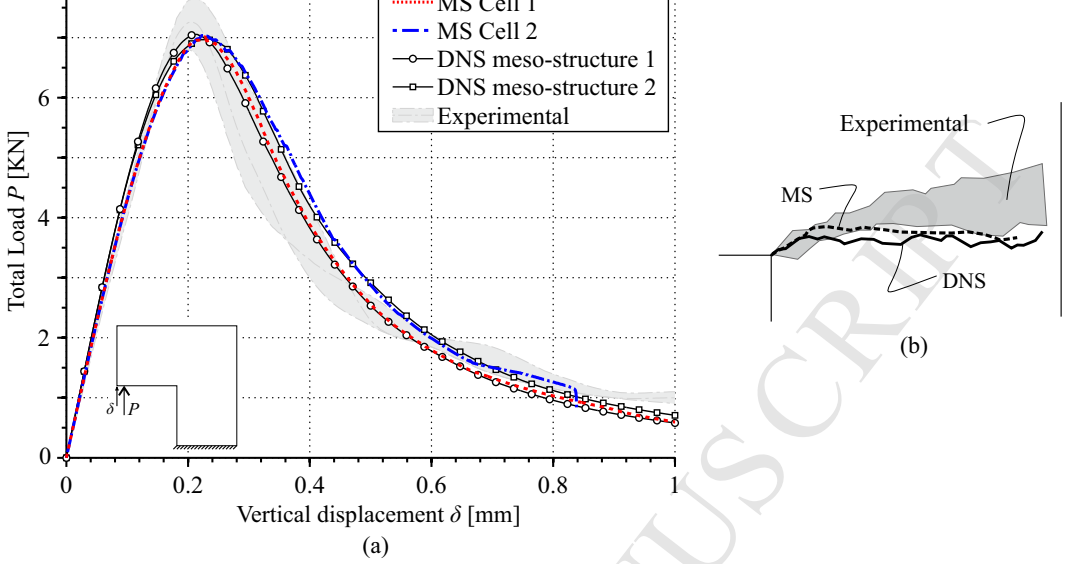

Figure 20: L-Panel test: (a) Load P vs vertical displacement δ curves, for MS, DNS and experiments. (b) Comparative analysis between numerical solutions (MS and DNS) vs. experimental envelope of the macro-scale crack paths.

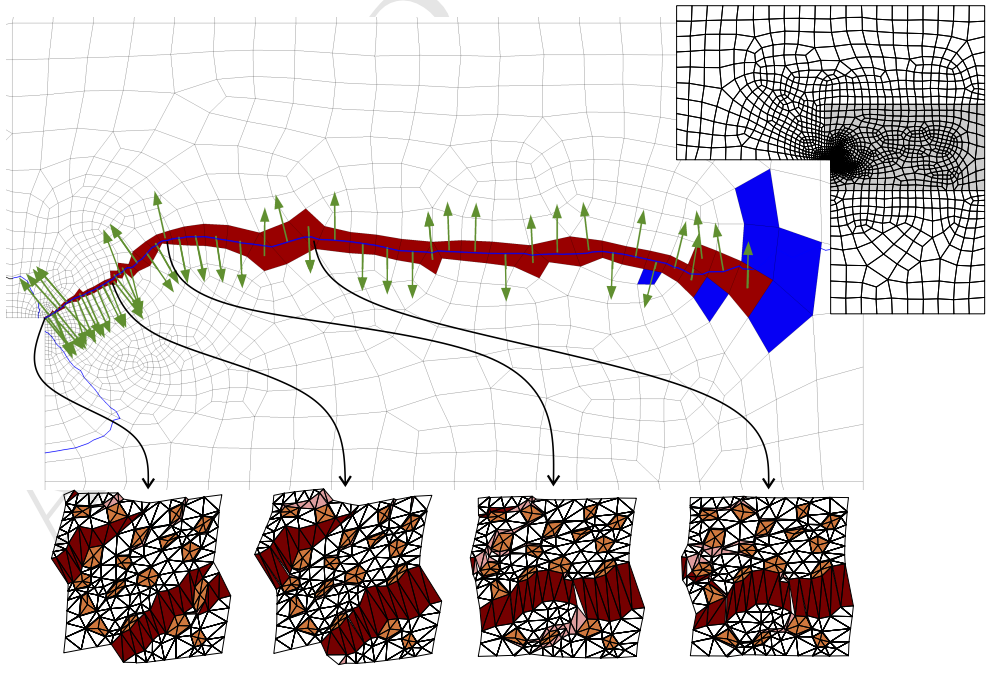

Figure 21: L-Panel test. Macro-scale solution using the multiscale (MS) model and Cell 1 (average size of the macro-scale finite elements in the crack propagation zone: 6.03 [mm]). Crack path, vector field normal to the cohesive surface and some deformed meso-structures at different points $\boldsymbol{x}_{\mathcal{S}}$ along the macroscopic cohesive crack. At the meso-scale, opening cohesive interfaces are shown in deep red, at $t = t_N$. Interfaces which have been opening during the loading process but they are closing at t_N are shown in light red.

been proposed. The method is based on the RVE-concept and follows a kinematical/variational setting. A particular feature is the axiomatization of the methodology, defining hypotheses and derived consequences of the formulation. Essential modeling phenomenologies have been incorporated invoking a minimum of additional assumptions. Specifically we refer to the introduction of the micro-scale crack tortuosity effect, a relevant mechanism to be considered in the context of failure modeling.

Novel aspects of the present multiscale methodology are:

- The definition of an insertion operator, $\boldsymbol{\mathcal{I}}(\cdot)$, which is appropriate for the challenging problem in question. This operator distributes the macro-scale regular kinematics and the macro-scale discontinuous kinematics in distinct ways within the RVE-domain, according with the phenomenology of localization taking place at the micro-scale. Insertion mechanism can be arbitrarily postulated under the premise that this procedure is linear and preserves the macro-scale kinematical quantity inserted at the micro-scale. In order to satisfy the second condition for $\boldsymbol{\mathcal{I}}(\cdot)$, we incorporate the tortuosity parameter, θ, in the definition of the insertion procedure. Therefore, in the present framework, the tortuosity-index is considered as a primary kinematical concept.

- Another ingredient of the model is the so-called kinematically admissibility requirement which imposes proper constraints to have full control over the involved fluctuation fields in the RVE. Kinematical admissibility defines the mathematical structure (function vector spaces) required to describe the mechanical coupling between both scales of analysis.

- The introduction of a specific variational Principle of Multiscale Virtual Power, an adapted version of the Hill-Mandel principle, closes the theoretical formulation of the multiscale model. From this principle, the equilibrium problem at the RVE level, as well as the corresponding homogenization formulae for stresses and cohesive tractions, are obtained by straightforward variational arguments.

An important result of the present work is the role played by the tortuosity-index. It affects the constitutive response of the macro-scale cohesive crack as well as the macro-scale stress tensor for points located near the crack. The implicit dependence (non-linear in general) between the tortuosity parameter and the homogenized mechanical responses is not an a priori postulate of the formulation, but a natural consequence of the variational setting of the problem, along with the kinematically-based assumptions.

This result is useful to improve the predictive capabilities in mono-scale modeling of material failure, due to crack propagation. Thus, in phenomenological models based on the cohesive crack method both constitutive relations, the continuum stress-strain model and the discrete cohesive law, should be adapted through the incorporation of an estimated measure of the tortuosity in the smaller length scales. From the ideas discussed here, the form in which such adaptation can be done is simple and consists of two steps: (i) to modify the kinematical quantities before invoking the phenomenological constitutive models, as suggested by the insertion mechanism of the present multiscale model (that is the macro-scale kinematical descriptors $d\boldsymbol{\varepsilon_\beta}$ and $d\boldsymbol{\beta}$ must be linearly affected by θ-index) and (ii) to affect (linearly) the cohesive traction, retrieved by the phenomenological traction-separation law, by the tortuosity parameter, as shown in the cohesive traction homogenization formula of the present multiscale model.

The multiscale modeling strategy has not only theoretical foundation but also it is numerically implemented into a FE^2 scheme. The resulting computational homogenization technique performs well when compared with DNS solutions, both qualitatively and quantitatively. The load-displacement structural curves, obtained with the multiscale technique, show accurate results in terms of overall initial elasticity, non-linear stable behavior, peak load detection and post-critical dissipation, allowing a good estimation of the effective fracture energy at the macro-scale. The failure modes at micro and macro-scales levels are fully consistent with the crack path predicted by the DNS approach.

Finally we highlight the theoretical framework for the scale transition technique proposed in [1, 2, 55] and generalized in the present work. This framework provides a methodology for modeling material failure within a multiscale RVE-based setting, irrespective of the *regularized constitutive method* used at the micro-scale to manipulate unstable materials featuring smeared cracks, cohesive cracks, etc.

631) and from the European Research Council under the European Unions Seventh Framework Programme (FP/2007-2013) / ERC Grant Agreement N. 320815 (ERC Advanced Grant Project Advanced tools for computational design of engineering materials COMP-DES-MAT). P.J. Blanco and R.A. Feijóo acknowledge the financial support provided by the Brazilian agencies CNPq and FAPERJ. E.A. de Souza Neto gratefully acknowledges the financial support from CNPq to his visits to LNCC as part of the Science without Borders Programme.

Appendix I: Additional issues of the multiscale model

This appendix describes specific aspects of the proposed multiscale formulation, which were not detailed in the main body of the manuscript.

I-(a) Strong discontinuity kinematics as a limit case of strain localization bands

For simplicity, the following developments assume the existence of a unique cohesive crack at the micro-scale. Thus, superscript "i" (related to each micro-crack in the RVE) as well as the summation-operator can be removed. It is assumed that the (fluctuation) displacement discontinuity kinematics in a micro-crack can be viewed as the limit case of a strain localization band with finite thickness ℓ_μ, when $\ell_\mu \to 0$. Accordingly, the (incremental fluctuation) strain field at the micro-scale, $d\tilde{\boldsymbol{\varepsilon}}_\mu$, is given by equation (23). To see this in detail, we first write a continuous kinematical description with strain localization bands and then find the limit when the band thickness tends to zero.

Consider the domain $\Omega_{\mathcal{S}_\mu}$ with mean surface $\mathcal{S}_\mu$ and finite thickness ℓ_μ (see Fig. 22-(a)). In the same figure, $\boldsymbol{n}_\mu$ is the unit vector normal to $\mathcal{S}_\mu$. The displacement fluctuation field, $d\tilde{\boldsymbol{u}}_\mu$, with a strain localization band across the domain $\Omega_{\mathcal{S}_\mu}$ can be expressed as:

$$d\tilde{\boldsymbol{u}}_\mu = d\tilde{\boldsymbol{u}}_\mu + \mathscr{M}_\mu^* \, d\tilde{\boldsymbol{\beta}}_\mu, \quad \forall\, \boldsymbol{y} \in \Omega_\mu, \tag{69}$$

where $d\tilde{\boldsymbol{u}}_\mu$ is the regular fluctuation and $(\mathscr{M}_\mu^* \, d\tilde{\boldsymbol{\beta}}_\mu)$ is an additional *continuous* fluctuation displacement mode related with the strain localization band. The function $\mathscr{M}_\mu^*$, introduced in (69), has the following definition:

$$\mathscr{M}_\mu^* := \mathscr{H}_\mu^* - \varphi_\mu^*, \tag{70}$$

$$\mathscr{H}_\mu^* = \begin{cases} 1 & \forall\, \boldsymbol{y} \in \Omega_{\mu+}^* \\ \frac{\boldsymbol{n}_\mu \cdot (\boldsymbol{y} - \boldsymbol{y}_0)}{\ell_\mu} & \forall\, \boldsymbol{y} \in \Omega_{\mathcal{S}_\mu} \\ 0 & \forall\, \boldsymbol{y} \in \Omega_{\mu-}^* \end{cases}, \quad \varphi_\mu^* = \begin{cases} 0 & \forall\, \boldsymbol{y} \in \Omega_{\mu-}^* \backslash \Omega_{\mu-}^{\varphi\,*} \\ 1 & \forall\, \boldsymbol{y} \in \Omega_{\mu+}^* \backslash \Omega_{\mu+}^{\varphi\,*}, \end{cases} \tag{71}$$

in terms of the ramp-function $\mathscr{H}_\mu^*$ (see (71)-left) and a continuous function φ_μ^* which satisfies (71)-right. The sets $\Omega_{\mu+}^*$, $\Omega_{\mu-}^*$, $\Omega_{\mu+}^{\varphi\,*}$ and $\Omega_{\mu+}^{\varphi\,*}$ have the geometrical interpretation given in Fig. 22-(a), where the $(\cdot)_+$ subscript is related to the $\boldsymbol{n}_\mu$-orientation. Point $\boldsymbol{y}_0$, in (71)-right, is an arbitrary point in the intersection $\Omega_{\mathcal{S}_\mu} \cap \Omega_{\mu-}^*$. Observe that $\Omega_\mu^{\varphi\,*}$ $(= \Omega_{\mu+}^{\varphi\,*} \cup \Omega_{\mu-}^{\varphi\,*})$ is an arbitrary small domain which includes the strain localization domain $\Omega_{\mathcal{S}_\mu}$.

With the previous definitions, the strain fluctuation $d\tilde{\boldsymbol{\varepsilon}}_\mu$, kinematically compatible with the field $d\tilde{\boldsymbol{u}}_\mu$ given by (69), reads:

$$d\tilde{\boldsymbol{\varepsilon}}_\mu = \nabla_y^s \, d\tilde{\boldsymbol{u}}_\mu + \mathscr{M}_\mu^* \, \nabla_y^s \, d\tilde{\boldsymbol{\beta}}_\mu - d\tilde{\boldsymbol{\beta}}_\mu \otimes^s \nabla_y \, \varphi_\mu^* + \phi_\mu \, \frac{d\tilde{\boldsymbol{\beta}}_\mu \otimes^s \boldsymbol{n}_\mu}{\ell_\mu}, \tag{72}$$

where the collocation function ϕ_μ is identical to (24), that is:

$$\phi_\mu = \begin{cases} 1 & \forall\, \boldsymbol{y} \in \Omega_{\mathcal{S}_\mu} \\ 0 & \text{otherwise.} \end{cases} \tag{73}$$

By taking the limit $\ell_\mu \to 0$ in (72), we obtain:

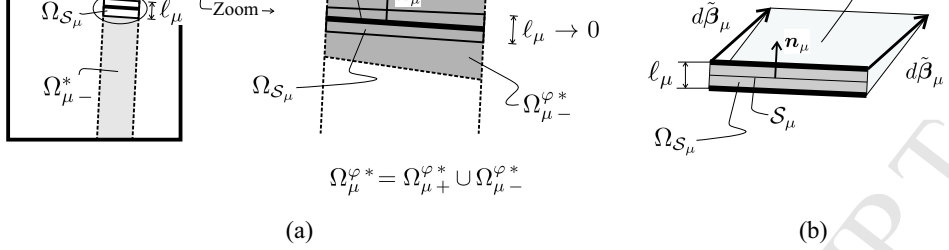

Figure 22: Basic nomenclature to describe a micro-scale kinematics with a strain localization band.

$$d\tilde{\boldsymbol{\varepsilon}}_\mu = \nabla^s_y\, d\tilde{\boldsymbol{u}}_\mu + \left[\lim_{\ell_\mu\to 0} \mathscr{M}^*_\mu\right] \nabla^s_y\, d\tilde{\boldsymbol{\beta}}_\mu - d\tilde{\boldsymbol{\beta}}_\mu \otimes^s \left[\lim_{\ell_\mu\to 0} \nabla_y\, \varphi^*_\mu\right] + \lim_{\ell_\mu\to 0} \phi_\mu\, \frac{d\tilde{\boldsymbol{\beta}}_\mu \otimes^s \boldsymbol{n}_\mu}{\ell_\mu}. \tag{74}$$

Then, considering the definitions (19), (20) and (22), expression (74) can be re-written as:

$$d\tilde{\boldsymbol{\varepsilon}}_\mu = \nabla^s_y\, d\tilde{\boldsymbol{u}}_\mu + \mathscr{M}_\mu\, \nabla^s_y\, d\tilde{\boldsymbol{\beta}}_\mu - d\tilde{\boldsymbol{\beta}}_\mu \otimes^s \nabla_y\, \varphi_\mu + \lim_{\ell_\mu\to 0} \phi_\mu\, \frac{d\tilde{\boldsymbol{\beta}}_\mu \otimes^s \boldsymbol{n}_\mu}{\ell_\mu} = d\tilde{\boldsymbol{\varepsilon}}_{\mu\,R} + \lim_{\ell_\mu\to 0} \phi_\mu\, \frac{d\tilde{\boldsymbol{\beta}}_\mu \otimes^s \boldsymbol{n}_\mu}{\ell_\mu}, \tag{75}$$

which proves the equivalence between equations (21) and (23), used in the paper, since the Dirac delta function can be viewed as:

$$\delta_\mu = \lim_{\ell_\mu\to 0} \frac{\phi_\mu}{\ell_\mu} \tag{76}$$

From a kinematical point of view, the strain-like term $\phi_\mu\, d\tilde{\boldsymbol{\beta}}_\mu \otimes^s \boldsymbol{n}_\mu\, (\ell_\mu)^{-1}$, in (75), is compatible with a displacement field displaying a strong discontinuity kinematics of magnitude $d\tilde{\boldsymbol{\beta}}_\mu$ across $\mathcal{S}_\mu$ (whose normal vector is $\boldsymbol{n}_\mu$) when $\ell_\mu \to 0$, see Fig 22-(b).

We also stress the following identity:

$$\int_{\Omega_\mu} \lim_{\ell_\mu\to 0} \frac{\phi_\mu}{\ell_\mu}\, f(\boldsymbol{y})\, d\Omega_\mu = \int_{\mathcal{S}_\mu} f(\boldsymbol{y})\, d\mathcal{S}_\mu \tag{77}$$

for any smooth function $f(\boldsymbol{y})$, which has been used throughout the paper.

I-(b) Procedure to determine the set of opening micro-cracks: $\mathcal{S}^L_\mu$

A critical point in the proposed multiscale formulation is the correct determination of the set of opening micro-cracks, here referred to as $\mathcal{S}^L_\mu$, at the macro-scale nucleation time $t = t_N$. Such interface sub-domain, $\mathcal{S}^L_\mu \subset \Omega_\mu$, must be properly captured for two main reasons:

(i) For $t > t_N$, the insertion mechanism of the macro-scale jump increment ($\boldsymbol{\mathcal{I}}(\boldsymbol{0}, \boldsymbol{0}, d\boldsymbol{\beta})$) into the micro-scale domain is restricted, exclusively, to the set $\mathcal{S}^L_\mu$ of opening micro-cracks (see equation (26)).

(ii) New constraints must be applied to the micro-scale incremental displacement jump fluctuations $d\tilde{\boldsymbol{\beta}}_\mu$, related to the set $\mathcal{S}^L_\mu$ (see expression (36)).

The procedure to determine $\mathcal{S}^L_\mu$ is based on a purely kinematical criterion. Let us consider the mechanical state of the RVE, at the macro-scale nucleation time $t = t_N$. Recall that t_N is determined according to the singularity of the acoustic tensor [1, 2, 55]. The solution to this problem gives $\{t_N, \boldsymbol{n}, \boldsymbol{\gamma}\}$, where $\boldsymbol{n}$ is the unit vector normal to the macro-scale cohesive crack and $\boldsymbol{\gamma}$ is the initial direction of the macro-scale displacement discontinuity, $d\boldsymbol{\beta}$, at t_N. Thus, at t_N, the mechanical state of the RVE is compatible with the nucleation of a macro-scale cohesive crack which has the *instantaneous* strain-like mode characterized by the tensor structure $(\boldsymbol{\gamma} \otimes^s \boldsymbol{n})$.

On the other hand, at t_N, there are n_c micro-scale cohesive interfaces $\mathcal{S}^i_\mu$ (with $i = 1, \ldots, n_c$) which have been nucleated in the RVE-domain up to time t_N. The set of all nucleated micro-cracks is $\mathcal{S}^T_\mu = \cup_{i=1}^{n_c} \mathcal{S}^i_\mu$.

strain-like term having the structure $(\boldsymbol{\gamma} \otimes^s \boldsymbol{n})$. Mathematically, this criterion can be expressed as:

$$\mathcal{S}_\mu^L = \big\{ \cup \mathcal{S}_\mu^i, \text{ such that } (d\tilde{\boldsymbol{\beta}}_\mu^i \otimes^s \boldsymbol{n}_\mu^i) \cdot (\boldsymbol{\gamma} \otimes^s \boldsymbol{n}) > 0,\ i = 1, \ldots, n_c, \text{ for } t = t_N \big\}. \tag{78}$$

Each micro-crack $\mathcal{S}_\mu^i$, whose corresponding $d\tilde{\boldsymbol{\beta}}_\mu^i$ satisfies the positive-projection rule given in (78), is considered to be an opening micro-crack $\mathcal{S}_\mu^{Lj}$ $(j = 1, \ldots, n_{op})$. The total number of opening micro-cracks is n_{op}. Conversely, micro-cracks $\mathcal{S}_\mu^i$ with $d\tilde{\boldsymbol{\beta}}_\mu^i$ such that do not satisfy the inequality in (78) form the set of closing cracks $(\mathcal{S}_\mu^T \backslash \mathcal{S}_\mu^L)$.

I-(c) Derivation of the tortuosity factor expression

We derive the expression (27) adopted for the tortuosity factor θ, introduced in the definition of the insertion operator $\boldsymbol{\mathcal{I}}(\cdot)$ (see equation (26)). The following argument is based on a purely kinematical constraint which should be satified by the insertion operator. In this sense, it is postulated:

$$\frac{1}{|\mathcal{S}_\mu^L|} \int_{\Omega_\mu^L} \overbrace{\left[\sum_{j=1}^{n_{op}} \lim_{\ell_\mu^{Lj} \to 0} \phi_\mu^{Lj} \, \frac{\theta \, d\boldsymbol{\beta} \otimes^s \boldsymbol{n}_\mu^{Lj}(\boldsymbol{y})}{\ell_\mu^{Lj}} \right]}^{\boldsymbol{\mathcal{I}}(\mathbf{0},\mathbf{0},d\boldsymbol{\beta})} d\Omega_\mu = d\boldsymbol{\beta} \otimes^s \boldsymbol{n}, \quad \forall\, d\boldsymbol{\beta}, \tag{79}$$

where $\Omega_\mu^L = \bigcup_{j=1}^{n_{op}} \Omega_\mu^{Lj}$, is the entire strain localization sub-domain associated to $\mathcal{S}_\mu^L$. The left hand side of (79) is the mean value of $\boldsymbol{\mathcal{I}}(\mathbf{0}, \mathbf{0}, d\boldsymbol{\beta})$. The right hand size of (79) represents the macro-scale kinematical descriptor related to $d\boldsymbol{\beta}$, which has the structure given by $d\boldsymbol{\beta} \otimes^s \boldsymbol{n}$.

Equation (79) can be further manipulated, leading to:

$$\begin{aligned}
\frac{1}{|\mathcal{S}_\mu^L|} \sum_{j=1}^{n_{op}} \int_{\Omega_\mu^{Lj}} \left[\delta_\mu^{Lj} \, \theta \, d\boldsymbol{\beta} \otimes^s \boldsymbol{n}_\mu^{Lj}(\boldsymbol{y}) \right] d\Omega_\mu &= d\boldsymbol{\beta} \otimes^s \boldsymbol{n}, \quad \forall\, d\boldsymbol{\beta}, \\
\frac{1}{|\mathcal{S}_\mu^L|} \sum_{j=1}^{n_{op}} \int_{\mathcal{S}_\mu^{Lj}} \left[\theta \, d\boldsymbol{\beta} \otimes^s \boldsymbol{n}_\mu^{Lj}(\boldsymbol{y}) \right] d\mathcal{S}_\mu &= d\boldsymbol{\beta} \otimes^s \boldsymbol{n}, \quad \forall\, d\boldsymbol{\beta}, \\
\frac{1}{|\mathcal{S}_\mu^L|} \theta \, d\boldsymbol{\beta} \otimes^s \sum_{j=1}^{n_{op}} \int_{\mathcal{S}_\mu^{Lj}} \boldsymbol{n}_\mu^{Lj}(\boldsymbol{y}) \, d\mathcal{S}_\mu &= d\boldsymbol{\beta} \otimes^s \boldsymbol{n}, \quad \forall\, d\boldsymbol{\beta}, \\
\frac{\theta}{|\mathcal{S}_\mu^L|} \sum_{j=1}^{n_{op}} \int_{\mathcal{S}_\mu^{Lj}} \boldsymbol{n}_\mu^{Lj}(\boldsymbol{y}) \, d\mathcal{S}_\mu &= \boldsymbol{n}.
\end{aligned} \tag{80}$$

Since $\boldsymbol{n}$ (the normal vector to the macro-scale cohesive crack) is a unit vector, expression (80) gives the criterion to compute the tortuosity factor θ, as follows:

$$\theta = \frac{|\mathcal{S}_\mu^L|}{\left| \sum_{j=1}^{n_{op}} \int_{\mathcal{S}_\mu^{Lj}} \boldsymbol{n}_\mu^{Lj}(\boldsymbol{y}) \, d\mathcal{S}_\mu \right|}, \quad \theta \in [1, \infty). \tag{81}$$

Remark 7.1 *Equation* (79) *is a kinematical constraint requiring that the insertion operator* $\boldsymbol{\mathcal{I}}(\mathbf{0}, \mathbf{0}, d\boldsymbol{\beta})$ *preserves the macro-scale kinematics, i.e. the* $(\boldsymbol{\beta} \otimes^s \boldsymbol{n})$ *term in this case. When the insertion operator has a simple definition, as in conventional multiscale models without discontinuities, this property is trivially satisfied. In more general modeling scenarios special care must be taken in the specification of* $\boldsymbol{\mathcal{I}}(\cdot)$*. Also note that the Kinematical Admissibility Concept (see* (31)-(33)*), does not necessarily takes into account this issue, since it only controls the RVE fluctuation fields.*

description assume a single micro-scale cohesive crack (superscript "i" and summation-operator are removed from the following equations). The present discussion distinguishes between the case of an internal crack or a crack reaching the RVE-boundary (see Fig. 3-(a)).

II-(a) Internal micro-crack

From (33) the first admissibility requirement is expressed as:

$$\mathbf{0} = \int_{\Omega_\mu} \left[d\tilde{\boldsymbol{\varepsilon}}_{\mu R} + \lim_{\ell_\mu \to 0} \phi_\mu \, \frac{d\tilde{\boldsymbol{\beta}}_\mu \otimes^s \boldsymbol{n}_\mu}{\ell_\mu} \right] d\Omega_\mu = \int_{\Omega_\mu} \left(d\tilde{\boldsymbol{\varepsilon}}_{\mu R} + \delta_\mu \, d\tilde{\boldsymbol{\beta}}_\mu \otimes^s \boldsymbol{n}_\mu \right) d\Omega_\mu, \tag{82}$$

and taking (22) into account, expression (82) is re-written as follows:

$$\mathbf{0} = \int_{\Omega_\mu} \big(\overbrace{\nabla_y^s \, d\tilde{\boldsymbol{u}}_\mu + \underbrace{\mathscr{M}_\mu \nabla_y^s \, d\tilde{\boldsymbol{\beta}}_\mu}_{\text{T1}} - \underbrace{d\tilde{\boldsymbol{\beta}}_\mu \otimes^s \nabla_y \varphi_\mu}_{\text{T2}}}^{d\tilde{\boldsymbol{\varepsilon}}_{\mu R}} + \underbrace{\delta_\mu \, d\tilde{\boldsymbol{\beta}}_\mu \otimes^s \boldsymbol{n}_\mu}_{\text{T3}} \big) \, d\Omega_\mu, \tag{83}$$

where the terms T1, T2 and T3 can be further manipulated. Considering the nomenclature shown in Fig. 3-(b), the term T1 can be expressed as:

$$\begin{aligned} \text{T1}: \int_{\Omega_\mu} \mathscr{M}_\mu \nabla_y^s \, d\tilde{\boldsymbol{\beta}}_\mu \, d\Omega_\mu &= \int_{\Omega_{\mu+}^\varphi} \nabla_y^s \, d\tilde{\boldsymbol{\beta}}_\mu \, d\Omega_\mu - \int_{\Omega_\mu^\varphi} \varphi_\mu \, \nabla_y^s \, d\tilde{\boldsymbol{\beta}}_\mu \, d\Omega_\mu \\ &= \int_{\mathcal{S}_{\mu+}} d\tilde{\boldsymbol{\beta}}_\mu \otimes^s \boldsymbol{n}_{\mu+} \, d\mathcal{S}_\mu - \int_{\mathcal{S}_\mu} d\tilde{\boldsymbol{\beta}}_\mu \otimes^s \boldsymbol{n}_\mu \, d\mathcal{S}_\mu - \int_{\Omega_\mu^\varphi} \varphi_\mu \, \nabla_y^s \, d\tilde{\boldsymbol{\beta}}_\mu \, d\Omega_\mu, \end{aligned} \tag{84}$$

where the definition of the micro-scale unit jump function $\mathscr{M}_\mu$ has been considered, together with a standard tensorial identity and the fact that the crack is internal to the RVE-domain, i.e. $d\tilde{\boldsymbol{\beta}}_\mu|_{\Gamma_{\mu I}^\varphi} = d\tilde{\boldsymbol{\beta}}_\mu|_{\Gamma_{\mu II}^\varphi} = \mathbf{0}$ and $\boldsymbol{n}_{\mu+}$ is the outward unit vector normal to $\mathcal{S}_{\mu+}$.

The term T2 is expanded as follows:

$$\begin{aligned} -\text{T2}: -\int_{\Omega_\mu} d\tilde{\boldsymbol{\beta}}_\mu \otimes^s \nabla_y \varphi_\mu \, d\Omega_\mu &= -\int_{\Omega_\mu^\varphi} \nabla_y^s (\varphi_\mu \, d\tilde{\boldsymbol{\beta}}_\mu) \, d\Omega_\mu + \int_{\Omega_\mu^\varphi} \varphi_\mu \, \nabla_y^s \, d\tilde{\boldsymbol{\beta}}_\mu \, d\Omega_\mu \\ &= -\int_{\mathcal{S}_{\mu+}} d\tilde{\boldsymbol{\beta}}_\mu \otimes^s \boldsymbol{n}_{\mu+} \, d\mathcal{S}_\mu + \int_{\Omega_\mu^\varphi} \varphi_\mu \, \nabla_y^s \, d\tilde{\boldsymbol{\beta}}_\mu \, d\Omega_\mu, \end{aligned} \tag{85}$$

where standard tensor identities have been considered along with the definition of φ_μ, given by (20)-right, and the internal crack concept.

The term T3 is evaluated from the properties of the Dirac delta function, yielding:

$$\text{T3}: \int_{\Omega_\mu} \delta_\mu \, d\tilde{\boldsymbol{\beta}}_\mu \otimes^s \boldsymbol{n}_\mu \, d\Omega_\mu = \int_{\mathcal{S}_\mu} d\tilde{\boldsymbol{\beta}}_\mu \otimes^s \boldsymbol{n}_\mu \, d\mathcal{S}_\mu. \tag{86}$$

From (84), (85) and (86), the integral expression (83) reduces to:

$$\mathbf{0} = \int_{\Omega_\mu} \nabla_y^s \, d\tilde{\boldsymbol{u}}_\mu \, d\Omega_\mu, \tag{87}$$

proving the equivalence between (33) and (34). Note that, although in the micro-scale there are two independent kinematical descriptors $\{d\tilde{\boldsymbol{u}}_\mu, d\tilde{\boldsymbol{\beta}}_\mu\}$, expression (87) (and (34)) imposes kinematical constraints only over the field $d\tilde{\boldsymbol{u}}_\mu$.

In this case, $d\boldsymbol{\beta}_\mu|_{\Gamma^\varphi_{\mu II}} \neq \mathbf{0}$. Integrals of the type:

$$\int_{\Gamma^\varphi_{\mu II}} (d\tilde{\boldsymbol{\beta}}_\mu \otimes^s \boldsymbol{n}_{\mu II})\, d\Gamma_\mu, \tag{88}$$

do not vanish in the above derivations of the terms T1 and T2. In (88), $\boldsymbol{n}_{\mu\, II}$ is the outward unit vector normal to $\Gamma^\varphi_{\mu\, II}$. Then, equivalence between (83) and (87) is no longer guaranteed. However let us recall that the sub-domain Ω^φ_μ, introduced to define the kinematical description of strong discontinuities at the micro-scale (see Section 3.2.1), has an arbitrarily small thickness in the orthogonal direction to the micro-crack $\mathcal{S}_\mu$. Thus the measure of $\Gamma^\varphi_{\mu II}$ (and also $\Gamma^\varphi_{\mu I}$) is also arbitrarily small. Since expression (88) has bounded integrand, this integral can be neglected if compared with integrals on $\mathcal{S}_\mu$. Summarizing, equivalence between (83) and (87) is established in an approximate sense.

References

[1] P.J. Sánchez, P.J. Blanco, A.E. Huespe, and R.A. Feijóo. Failure-oriented multi-scale variational formulation: micro-structures with nucleation and evolution of softening bands. *Computer Methods in Applied Mechanics and Engineering*, 257:221–247, 2013.

[2] S. Toro, P.J. Sánchez, A.E. Huespe, S.M. Giusti, P.J. Blanco, and R.A. Feijóo. A two-scale failure model for heterogeneous materials: numerical implementation based on the finite element method. *Int. J. Num. Meth. Eng.*, 97:313–351, 2014.

[3] P.J. Blanco, P.J. Sánchez, E.A. de Souza Neto, and R.A. Feijóo. Variational foundations and generalized unified theory of RVE-based multiscale models. *Archives of Computational Methods in Engineering*, Accepted. DOI: 10.1007/s11831-014-9137-5, 2014.

[4] A. Needleman. Some issues in cohesive surface modeling. *Procedia IUTAM*, 10:221–246, 2013.

[5] Z. Zhang and G.H. Paulino. Cohesive zone modeling of dynamic failure in homogeneous and functionally graded materials. *International Journal of Plasticity*, 21(6):1195–1254, 2005.

[6] G. Pijaudier-Cabot and Z. Bazant. Nonlocal damage theory. *ASCE J. Engrg. Mech.*, 113(10):1512–1533, 1987.

[7] E. Aifantis. On the role of gradients in the localization of deformation and fracture. *J. Engrg Sci.*, 30:1279–1299, 1984.

[8] J. Mroginski, G. Etse, and S.M. Vrech. A thermodynamical gradient theory for deformation and strain localization of porous media. *International Journal of Plasticity*, 27(4):620–634, 2011.

[9] J. Oliver, M. Cervera, and O. Manzoli. Strong discontinuities and continuum plasticity models: the strong discontinuity approach. *International Journal of Plasticity*, 15(3):319–351, 1999.

[10] J. Oliver. On the discrete constitutive models induced by strong discontinuity kinematics and continuum constitutive equations. *Int. J. Solids Struct.*, 37:7207–7229, 2000.

[11] J. Oliver, A. E. Huespe, M. D. G. Pulido, and E. Chaves. From continuum mechanics to fracture mechanics: the strong discontinuity approach. *Engineering Fracture Mechanics*, 69:113–136, 2002.

[12] A.E. Huespe, A. Needleman, J. Oliver, and P.J. Sánchez. A finite strain, finite band method for modeling ductile fracture. *International Journal of Plasticity*, 28(1):53–69, 2011.

[13] M.F. Horstemeyer and D.J. Bammann. Historical review of internal state variable theory for inelasticity. *International Journal of Plasticity*, 26(9):1310–1334, 2010.

[14] F.P. Duda, A. Ciarbonetti, P.J. Sánchez, and A.E Huespe. A phase-field/gradient damage model for brittle fracture in elastic-plastic solids. *International Journal of Plasticity*, 65:269–296, 2015.

[15] P.M. Mariano. Multifield theories in mechanics of solids. *Advances in Applied Mechanics*, 38(C):1–93, 2002.

[16] S. Nemat-Nasser and M. Hori. *Micromechanics: overall properties of heterogeneous materials*. Elsevier, 1999.

[17] D.L. McDowell. A perspective on trends in multiscale plasticity. *International Journal of Plasticity*, 26:1280–1309, 2010.

[18] R. Hill. Elastic properties of reinforced solids: some theoretical principles. *J. Mech. Phys. Solids*, 11:357–372, 1963.

[19] R. Hill. A self-consistent mechanics of composite materials. *J. Mech. Phys. Solids*, 13:213–222, 1965.

[20] R. Hill. Continuum micro-mechanics of elastoplastic polycrystals. *J. Mech. Phys. Solids*, 13(2):89–101, 1965.

Phys. Solids, 11:127–140, 1963.

[23] B. Budiansky. On the elastic moduli of some heterogeneous materials. *J. Mech. Phys. Solids*, 13:223–227, 1965.

[24] J.D. Eshelby. The determination of the field of an ellipsoidal inclusion and related problems. *Proc. R. Soc. Lond A*, 241: 376–396, 1957.

[25] T. Mori and K. Tanaka. Average stress in the matrix and average energy of materials with misfitting inclusions. *Acta Metall.*, 21:571–574, 1973.

[26] R.M. Christensen and K.H. Lou. Solutions for effective shear properties in three phase sphere and cylinder models. *J. Mech. Phys. Solids*, 27:315–330, 1979.

[27] J.R. Willis. Variational and related methods for the overall properties of composites. *Adv. Apll. Mech.*, 21:1–78, 1981.

[28] E. Sanchez-Palencia. *Non-homogeneous media and vibration theory. Volume 127 on Lecture Notes in Physics*. Springer-Verlag, Berlin, 1980.

[29] J. Fish, Q. Yu, and K. Shek. Computational damage mechanics for composite materials based on mathematical homogenization. *Int. J. Numer. Meth. Engrg.*, 45:1657–1679, 1999.

[30] E.A. de Souza Neto and R.A. Feijóo. On the equivalence between spatial and material volume averaging of stress in large strain multi-scale solid constitutive models. *Mechanics of Materials*, 40:803–811, 2008.

[31] D. Perić, E.A. de Souza Neto, R.A. Feijóo, M. Partovi, and A.J. Carneiro Molina. On micro-to-macro transitions for multi-scale analysis of non-linear heterogeneous materials: unified variational basis and finite element implementation. *Int. J. Num. Meth. Eng.*, 87:149–170, 2011.

[32] E.A. de Souza Neto and R.A. Feijóo. Variational foundations of large strain multiscale solid constitutive models: Kinematical formulation. In M. Vaz, E.A. de Souza Neto, and P.A. Muoz-Rojas, editors, *Advanced Computational Materials Modeling. From Classical to Multi-Scale Techniques*, pages 341–378, Weinheim, 2011.

[33] I. Temizer and P.Wriggers. Homogenization in finite thermoelasticity. *J. Mech. Phys. Solids*, 59:344–372, 2012.

[34] F. Fritzena, S. Forest, T. Bohlkea, D. Kondoc, and T. Kanitd. Computational homogenization of elasto-plastic porous metals. *International Journal of Plasticity*, 29:102–119, 2012.

[35] Z. Li and P. Steimann. Rve-based studies on the coupled effects of void size and void shape on yield behavior and void growth at micron scales. *International Journal of Plasticity*, 22(7):1195–1216, 2006.

[36] C. Miehe and A. Koch. Computational micro-to-macro transition of discretized microstructures undergoing small strain. *Arch. Appl. Mech.*, 72:300–317, 2002.

[37] V.G. Kouznetsova, M.G.D. Geers, and W.A.M. Brekelmans. Multi-scale second-order computational homogenization of multi-phase materials: A nested finite element solution strategy. *Comput. Meth. App. Mech. Eng.*, 193:5525–5550, 2002.

[38] F. Feyel and J.L. Chaboche. Fe^2 multiscale approach for modelling the elastoviscoplastic behaviour of long fibre SiC/Ti composite materials. *Comput. Meth. App. Mech. Eng.*, 183:309–330, 2000.

[39] M Holl, S Loehnert, and P Wriggers. An adaptive multiscale method for crack propagation and crack coalescence. *International Journal for Numerical Methods in Engineering*, 93(1):23–51, 2013.

[40] O Lloberas-Valls, DJ Rixen, A Simone, and LJ Sluys. Multiscale domain decomposition analysis of quasi-brittle heterogeneous materials. *International Journal for Numerical Methods in Engineering*, 89(11):1337–1366, 2012.

[41] I.M. Gitman, H. Askes, and L.J. Sluys. Representative volume: Existence and size determination. *Engineering Fracture Mechanics*, 74:2518–2534, 2007.

[42] V.P. Nguyen, O.L. Valls, M. Stroeven, and L.J. Sluys. On the existence of representative volumes for softening quasi-brittle materials - a failure zone averaging scheme. *Computer Methods in Applied Mechanics and Engineering*, 199:3028–3038, 2010.

[43] Z.P. Bazant. *Scaling of structural strength.* Butterworth-Heinemann, 2005.

[44] J.H. Song and T. Belytschko. Multiscale aggregating discontinuities method for micro-macro failure of composites. *Composites*, Part B 40:417–426, 2009.

[45] T. Belytschko, S. Loehnert, and J.H. Song. Multiscale aggregating discontinuities: A method for circumventing loss of material stability. *Int. J. Numer. Meth. Engng.*, 73:869–894, 2008.

[46] V.P. Nguyen, O.L. Valls, and L.J. Sluys M. Stroeven. Homogenization-based multiscale crack modelling: from micro diffusive damage to macro cracks. *Computer Methods in Applied Mechanics and Engineering*, 200:1220–1236, 2010.

[48] K. Matous, M.G. Kulkarni, and P.H. Geubelle. Multiscale cohesive failure modeling of heterogeneous adhesives. *Journal of the Mechanics and Physics of Solids*, 56:1511–1533, 2008.

[49] E.W.C Coenen, V.G. Kouznetsova, and M.G.D. Geers. Novel boundary conditions for strain localization analyses in microstructural volume elements. *Int. J. Num. Meth. Eng.*, in press, 2011.

[50] C.V. Verhoosel, J.J.C. Remmers, M.A. Gutiérrez, and R. de Borst. Computational homogenization for adhesive and cohesive failure in quasi-brittle solids. *Int. J. Num. Meth. Eng.*, 83:1155–1179, 2010.

[51] M.G.D. Geers, V.G. Kouznetsova, and W.A.M. Brekelmans. Multi-scale computational homogenization: Trends and challenges. *Journal of Computational and Applied Mathematics*, 234:2175–2182, 2010.

[52] Caglar Oskay and Jacob Fish. Eigendeformation-based reduced order homogenization for failure analysis of heterogeneous materials. *Computer Methods in Applied Mechanics and Engineering*, 196(7):1216–1243, 2007.

[53] J. Oliver, M. Caicedo, E. Roubin, A.E. Huespe, and J.A. Hernández. Continuum approach to computational multiscale modelling of propagating fracture. *Comput. Meth. App. Mech. Eng.*, 2015. In press.

[54] J. Mandel. *Plasticit Classique at Viscoplasticit. CISIM Lecture Notes*. Springer-Verlag, 1971.

[55] P.J. Sánchez, P.J. Blanco, A.E. Huespe, and R.A. Feijóo. Failure-oriented multi-scale variational formulation for softening materials. Technical Report P&D N°6, LNCC-MCTI Laboratório Nacional de Computação Científica, 2011.

[56] M.A. Issa, M.A. Issa, M.S. Islam, and A. Chudnovsky. Fractal dimension a measure of fracture roughness and toughness of concrete. *Engineering Fracture Mechanics*, 70(1):125–137, 2003.

[57] J. Simo and J. Oliver. A new approach to the analysis and simulation of strain softening in solids. In Z.B. Bazant, Z. Bittnar, M. Jirásek, and J. Mazars, editors, *Fracture and Damage in Quasi-brittle Structures*, pages 25–39. E & FN Spon, 1994.

[58] E.A. de Souza Neto and R. Feijóo. Variational foundations of multi-scale constitutive models of solids: small and large strain kinematical formulation. Technical report, LNCC, Laboratório Nacional de Computação Científica, 2006.

[59] E.A. de Souza Neto, P.J. Blanco, P.J. Sánchez, and R.A. Feijóo. An RVE-based multiscale theory of solids with micro-scale inertia and body force effects. *Mechanics of Materials*, 80:136–144, 2015.

[60] J. Rudnicki and J. Rice. Condition for the localization of deformations in pressure sensitive dilatant materials. *J. Mech. Phys. Solids*, 23:371–394, 1975.

[61] J. Rice. The localization of plastic deformation. In W. Koiter, editor, *Theoretical and Applied Mechanics, 14th IUTAM Congress*, pages 207–220, Amsterdam, North-Holland, 1976.

[62] K. Runesson, N.S. Ottosen, and D. Peric. Discontinuous bifurcations of elastic-plastic solutions at plane stress and plane strain. *Int. J. of Plasticity*, 7:99–121, 1991.

[63] M.G. Kulkarni, P.H. Geubelle, and K. Matous. Multi-scale modeling of heterogeneous adhesives: Effect of particle decohesion. *Mechanics of Materials*, 41:573–583, 2009.

[64] V. Tvergaard and J.W. Hutchinson. The relation between crack growth resistance and fracture process parameters in elasto-plastic solids. *J. of the Mech. Phys. Solids*, 40:1377–1397, 1992.

[65] A.E. Huespe, J. Oliver, M.D.G. Pulido, S. Blanco, and D. Linero. On the fracture models determined by the continuum-strong discontinuity approach. *International Journal of Fracture*, 137(1-4):211–229, 2006.

[66] J. Oliver, I.F. Dias, and A.E. Huespe. Crack-path field and strain-injection techniques in computational modeling of propagating material failure. *Computer Methods in Applied Mechanics and Engineering*, 274:289–348, 2014.

[67] S. Toro, P.J. Blanco P.J. Sánchez, J.M. Podestá, A.E. Huespe, and R.A. Feijóo. Multiscale cohesive surface methodology for fracture problems: computational implementation. To be submitted, 2015.

[68] O.L. Manzoli, A.L. Gamino, E.A. Rodrigues, and G.K.S. Claro. Modeling of interfaces in two-dimensional problems using solid finite elements with high aspect ratio. *J. Computers & Structures*, 94:70–82, 2012.

[69] J. Oliver and A.E. Huespe. Theoretical and computational issues in modelling material failure in strong discontinuity scenarios. *Comput. Meth. App. Mech. Eng.*, 193:2987–3014, 2004.

[70] I. Carol, , C.M. López, and O. Roa. Micromechanical analysis of quasi-brittle materials using fracture-based interface elements. *International Journal for Numerical Methods in Engineering*, 52(1-2):193–215, 2001.

[71] J.F. Unger and S. Eckardt. Multiscale modeling of concrete. *Archives of Computational Methods in Engineering*, 18(3): 341–393, 2011.

[72] B. Winkler, G. Hofstetter, and G. Niederwanger. Experimental verification of a constitutive model for concrete cracking. *Proceedings of the Institution of Mechanical Engineers, Part L: Journal of Materials Design and Applications*, 215(2):75–86, 2001.

addressed.

• Effective cohesive laws are derived from solutions of micro-scale heterogeneous mechanical problems.

• The model accounts for a strong coupling between micro and macro cohesive cracks.

• Microscopic crack tortuosity is introduced as a kinematical concept having consequences on the homogenized responses.

• Using this formulation, a two-scale model for concrete fracture problems has been developed and tested.

• Model validation is performed by comparing with solutions obtained through Direct Numerical Simulations.